SEARCH FOR NON-YRAST STATES IN ^{160}Yb

Thifhelimbilu Daphney Singo

Thesis presented for the degree of Masters of Science

In the Department of Physics
University of Cape Town

Supervisor: **Prof David Aschman**
Department of Physics
University of Cape Town

Co-supervisor: **Dr Robert Bark**
iThemba Labs

19 May 2008

I would like to dedicate this work to my mother, Mrs Nyawasedza Fulufhedzani Singo.

Declaration

I declare that *The search for non-yrast states in* ^{160}Yb is my own work, that has not been submitted for any degree or examination in any other university, and that all the sources I have used or quoted have been acknowledged by complete references.

THIFHELIMBILU DAPHNEY SINGO

SIGNED:..... 19 May 2008

Abstract

The search for the theoretically predicted tetrahedral states has been the source of much interest in recent years with studies of the nuclear structure at low spin states. In this work we have looked for low spin non-yrast states of the even-even nucleus ^{160}Yb populated through the electron capture or β^+-decay of ^{160}Lu. The radioactive ^{160}Lu source was created through the heavy-ion fusion evaporation reaction ^{144}Sm(^{19}F,3n) at a beam energy of 85 MeV. Both γ-γ coincidences and single γ rays were detected using the AFRODITE Ge detector array at iThemba LABS. The computer program EONS was developed to measure the half-life of single γ rays for identification. The level scheme constructed from the γ-γ coincidence and single γ ray measurements confirms the existing level structure of ^{160}Yb. Population of low spin states was success and two new levels have been found, the 1755 keV level decays by a 1512 keV γ ray and 1825 kev level decays through 1582 keV.

Acknowledgements

- I would like to send my gratitude to MANDELA RHODES Foundation for the opportunity they gave me to be one of the 2007 scholars and the funding that made it possible for me to study this degree.
- My supervisor, Prof David Aschman, thank you so much for all the encouragement and support.

- I would like to specially thank my co-supervisor Dr Robert Bark. He patiently guided me on the project from time we ran the experiment, data analysis and the thesis.
- I gratefully acknowledge the efforts of the AFRODITE physics group and the technical staff at iThemba LABS.
- Finally, I give many thanks to my parents, my brothers and sister for all the support and encouragement and not forgetting my friends.

Contents

List of Figures

Chapter 1

Introduction

Nuclear structure is often described by independent particle models. These models assume that the effects of the internucleon interaction can be represented by a single particle potential. In shell models of the nucleus, the shape depends on the total energy obtained by filling the available orbitals, as a function of deformation. Thus in the spherical shell model when a shell of protons or neutrons is completely filled, having a maximum number of protons or neutrons allowed by the Pauli exclusion principle, the nucleus will take a spherical shape; for example ^{40}Ca has proton number $Z = 20$ and neutron number $N = 20$. Deformed shapes arise because the nucleus can lower its energy somewhat by rearranging its protons and neutrons into a deformed shell. The combination of the short-range nuclear force, Coulomb repulsion and Coriolis forces acting between neutrons and protons influences the shape of the nucleus. The deformed nuclei can have the well known quadrupole shape, in which the shape is either prolate or oblate. Nuclei can also take an octupole shape or perhaps the yet unobserved tetrahedral deformed shape.

This research focuses on nuclear structure of the deformed nucleus at a low spin. We aim to look for the theoretically predicted tetrahedral states of the nucleus ^{160}Yb. However the experimental evidence of this configuration is not conclusive, even though the calculations show that the nucleus ^{160}Yb is the best candidate to observe the stable tetrahedral shape [Dud03]. Tetrahedral states are predicted to lie at low spins above the ground state [Dud03]. There are several methods to populate low spin non-yrast states of nuclei including compound nuclear reactions and the β-decay process, but, because the tetrahedral states are expected to be at relatively low spins but possibly high excitation energy, we used β^+-decay. The low spin state of ^{160}Yb was then populated through the β^+-decay or electron capture of ^{160}Lu.

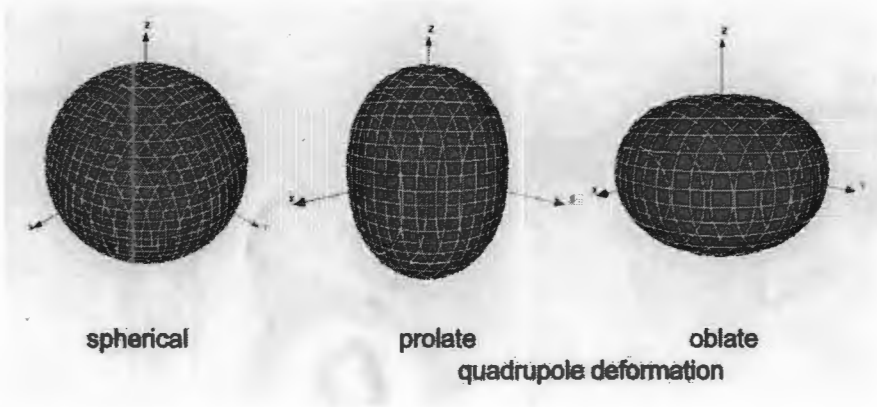

Figure 1.1: The different shapes of nuclei: spherical with no deformation, prolate and oblate deformed.

1.1 Thesis layout

In this work we present the results of research for tetrahedral states using electron capture or β^+-decay. In order to be able to understand and interpret the results obtained from the experiment we had to first understand the signature of tetrahedral rotational bands. The review of the theoretical predictions of where the tetrahedral states are expected to be found and how the rotational bands should look is discussed in chapter 1. Beta-decay experiments to populate low spin states have been performed previously and the level scheme of ^{160}Yb has been built, so in this work we also review the latest experiments of β-decay. Since this experiment was performed at iThemba LABS (Laboratory for Accelerator Based Sciences) we also review the achievements of the AFRODITE group in the search for the low spin state of the nucleus ^{160}Yb. These review studies of low spin states in ^{160}Yb using the β-decay and in-beam γ spectroscopy are described in chapter 2. It is very significant to have the knowledge of what could be expected from the experiment. In this regard the theoretical calculations for the experiment and the preparation of the parent nucleus ^{160}Lu were performed and they are presented in chapter 3. The computer program EONS was employed to extract the accurate half-life measurements of the single γ-ray's half-lives. This is discussed in the data analysis procedure in chapter 4. The level schemes of ^{160}Yb have been built from γ-γ coincidences and single γ-ray's data, the details of which are given in chapter 5. The half-life measurements results has been presented in table 5.1. Finally, the conclusions of the present study are discussed in chapter 6.

Figure 1.2: Octupole deformed shape of nucleus, with multipolarity $\lambda = 3$, $\mu = 0$.

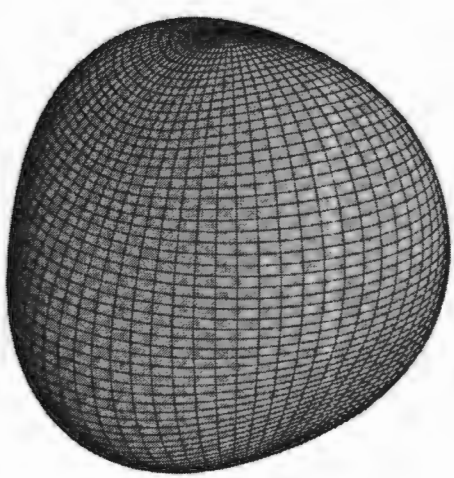

Figure 1.3: The calculated tetrahedral deformed shapes of the nucleus [Dud07].

1.2 Nuclear surface deformations

The nuclear shape is normally parametrized using the standard expansion [Nil95] in the basis of spherical harmonics $Y_{\mu\lambda}(\theta, \phi)$

$$R(\theta, \phi) = R_0 c(\alpha)[1 + \Sigma_\lambda \Sigma_\mu \alpha_{\lambda\mu} Y_{\lambda\mu}(\theta, \phi)], \tag{1.1}$$

where $R_0 = r_0 A^{1/3}$, r_0 is the radius of the nucleus and A is the mass number, $R(\theta, \phi)$ is the distance from the center of the nucleus to the surface at angles (θ, ϕ), $c(\alpha)$ accounts for the volume conservation when deforming the nucleus, and $\alpha_{\lambda\mu}$ are the deformation parameters, where $\alpha \equiv \{\alpha_{\lambda,\mu};\ \lambda = 0, 1, 2, 3, ...\lambda_{max};\ \mu = \pm\lambda\}$. The deformation parameter $\alpha_{0\mu}$ describes the monopole shape, where the nucleus has spherical shape, while $\alpha_{2\mu}$ describes the well-known quadrupole mode, where the shape of the nucleus can be either a prolate or oblate ellipsoid as seen in figure 1.1. Spherically shaped nuclei have zero quadrupole moment $Q_0 = 0$, while prolate and oblate shaped nuclei have positive $Q_0 > 0$ and negative $Q_0 < 0$ quadrupole moment respectively. Figure 1.2 shows the octupole α_{30} shape of the nucleus that looks like a pear. The tetrahedral shape with $\lambda = 3$ and $\mu = 2(\alpha_{\lambda\mu})$ is considered as a special case of an octupole mode. When a nucleus with tetrahedral shape is introduced in terms of the standard spherical harmonics Y_{32}, the deformation parameter α_{32} is non-zero. The calculated shape of a tetrahedral nucleus using standard spherical harmonics is shown in figure 1.3.

1.3 Tetrahedral shell gaps

The possible existence, at low spin, of nuclei with exotic shapes that resemble round-edge pyramids with tetrahedral symmetry has been theoretically predicted by Dudek *et al.* [Dud02]. The nuclear mean field calculations suggest the existence of magic numbers (shell gaps) associated with tetrahedral symmetry [Dud03]. The predicted magic numbers corresponding to particularly large gaps in the nucleonic single-particle spectra for protons are $Z = 16, 20, 32, 40, 56, 70, 90, 100, 112$ and 126, and for neutrons $N = 16, 20, 32, 40, 56, 70, 90, 100, 112$ and 136. This shows that there exist magic tetrahedral gaps throughout the periodic table. An example of single particle proton spectra as a function of the tetrahedral deformation is shown in figure 1.4. The deformed shell gaps are similar for protons and neutrons and are appropriate for medium heavy mass nuclei. The deformed shell gaps at proton number $Z = 70$ and neutron number $N = 90$, suggest the presence of extra stability associated with

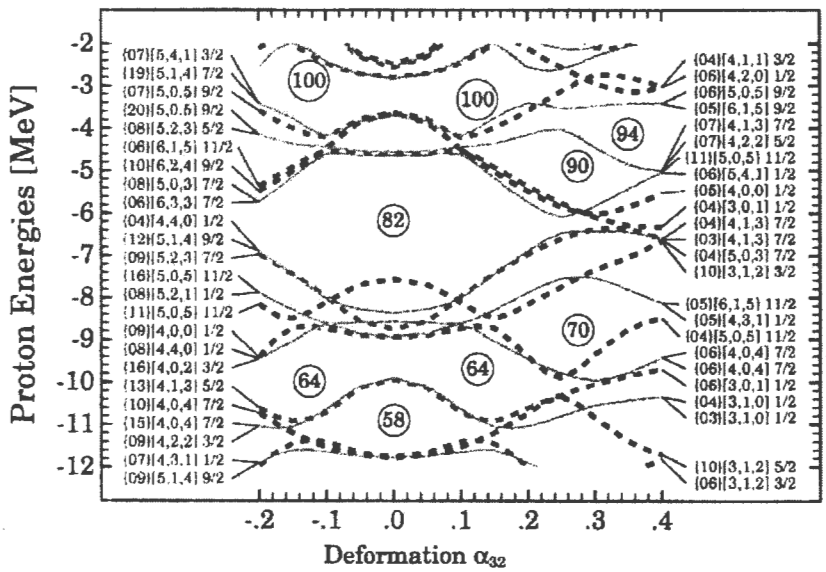

Figure 1.4: The single particle proton spectra as a function of the tetrahedral deformation of first order. Note the large gaps at $Z = 70$ and $90/94$ [Dud02].

a tetrahedral shape having $\alpha_{32} \sim 0.3$ near the nucleus ^{160}Yb.

Figure 1.5 shows the predicted [Dud06] energy difference between the normal E_{nd} and tetrahedral E_t deformation minima as a function of N and Z. Each brick represents 1 MeV of energy. This confirms that the nucleus with tetrahedral shape should lie low in excitation energy in the vicinity of the ^{160}Yb with $Z = 70$ and $N = 90$.

1.4 Collective excitations

The intrinsic states are the excited states upon which the new rotational bands can be built. They are intrinsic states because they reflect the intrinsic structure of the nucleus. Examples of intrinsic states are vibrational states and pair breaking particle excitations. Vibrational states occur when the nucleus vibrates about a deformed equilibrium shape. When the intrinsic states have spin projection K different from zero, a rotational band built on that state will have the sequence of spins $I, I+1, I+2, \ldots$, but for $K = 0$ the rotational band built on that state will have the sequence of spin $I, I+2, I+4, \ldots$. The most common nuclear vibrational states are octupole and quadrupole vibrations.

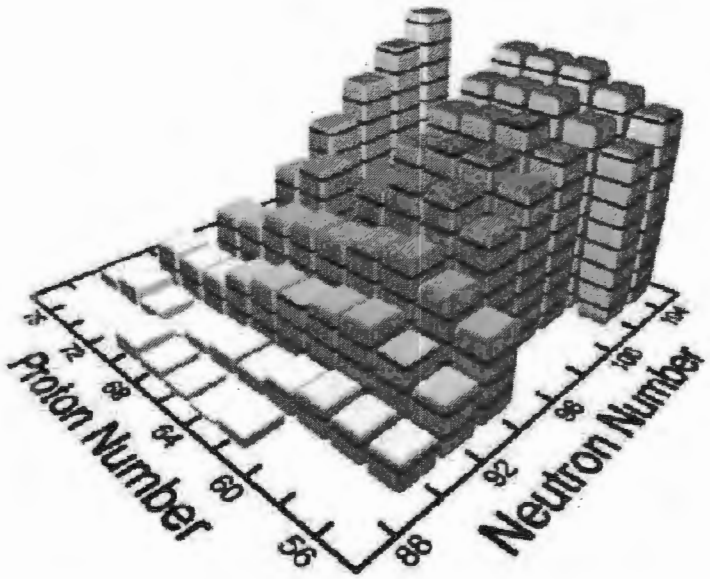

Figure 1.5: Energy difference $\Delta E = E_{\mathrm{t}} - E_{\mathrm{nd}}$ [Dud06].

1.4.1 Collective Rotation

The rotational motion is another possible mode of excitation in the quadrupole deformed nucleus. In the spherical case, it is not possible to observe collective rotation about the axis of symmetry, since the different orientations of the nucleus are quantum mechanically indistinguishable. This means that in quantum mechanics a wave function representing a spherical symmetric nucleus has no preferred of direction in space and the rotation does not show any noticeable change.

In the case of an axially-symmetric prolate or oblate nucleus, there is a set of axes of rotation perpendicular to the symmetry axis. The rotational angular momentum $\mathbf{R}$ is generated by the collective motion of many nucleons about the axis perpendicular to the symmetry axis. Additional angular momentum can be generated by the intrinsic angular momentum of any valence nucleons, $\mathbf{J}$. The total angular momentum $\mathbf{I}$ of the nucleus is then:

$$\mathbf{I} = \mathbf{R} + \mathbf{J}. \tag{1.2}$$

The angular momentum coupling is shown schematically in figure 1.6. The intrinsic angular momentum of the valence nucleons, $\mathbf{J}$, is the sum of the angular momentum of the individual valence nucleons, that is $\mathbf{J} = \sum_{i=1}^{A} \mathbf{j}_i$. The projection of the total angular momentum onto the symmetry axis is K, and is the same as the projection of $\mathbf{J}$. The projection of the angular

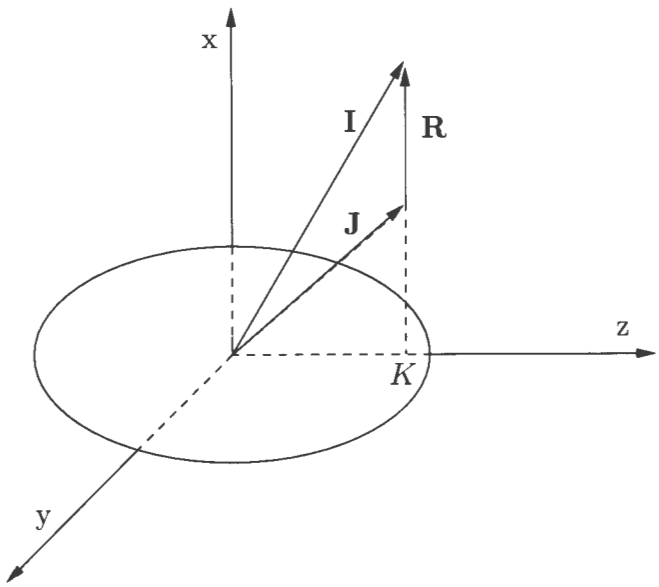

Figure 1.6: Schematic diagram illustrating the coupling of the collective angular momentum, **R** and the intrinsic angular momentum of the valence nucleons, **J**. K is the projection of the total angular momentum onto the symmetry axis.

momentum $\mathbf{j_i}$ of a valence nucleon is Ω_i; thus $M = \sum_{i=1}^{A} \Omega_i$.

For even-even nuclei, the nucleons in the nucleus couple to give a $\mathbf{J} = 0^+$ in the ground state. The rotational angular momentum **R** is the same as the total angular momentum **I**, for $K = 0$ and the angular part of the wave function which describes the rotation of the state, a spherical harmonic $Y_I^M(\theta, \phi)$, where M is the laboratory projection.

The parity of the wave function is positive. Because of the symmetry of an ellipsoid about an axis perpendicular to its symmetry axis, the sequence of allowed rotational states contains only even I, and so, this gives a set of levels with $I = 0^+, 2^+, 4^+, 6^+, \ldots$. The rotational angular momentum is given by $\mathcal{I}\omega$, where $\mathcal{I}$ is the effective moment of inertia and ω is the angular frequency of the rotation. The collective rotational energy can be determined through analogy with a classical rotating rigid body. The classical kinetic energy of the rotating rigid body is $\frac{1}{2}\mathcal{I}\omega^2$. By analogy to the quantum mechanics case, this becomes:

$$E_{rot} = \frac{(\mathcal{I}\omega)^2}{2\mathcal{I}} = \frac{\mathbf{I}^2}{2\mathcal{I}}. \tag{1.3}$$

Substituting the quantum mechanics result for the expectation value of the square of the

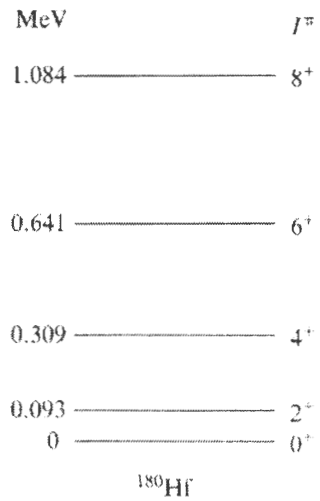

Figure 1.7: Low-lying level spectrum of the nucleus ^{180}Hf showing a band of states typical of a rotating, deformed nucleus with an axially symmetric quadrupole deformation [Kra88].

total angular momentum $\left\langle \hat{I}^2 \right\rangle = I(I+1)\hbar^2$ we obtain:

$$E(I) = \frac{I(I+1)\hbar^2}{2\mathcal{I}}. \tag{1.4}$$

Then the rotational motion of the nucleus leads to a sequences of states with energies

$$E(0^+) = 0, \tag{1.5}$$

$$E(2^+) = 6\frac{\hbar^2}{2\mathcal{I}}, \tag{1.6}$$

$$E(4^+) = 20\frac{\hbar^2}{2\mathcal{I}}. \tag{1.7}$$

Figure 1.7 shows the excited states of a typical rotational nucleus. The internal structure of the nucleus can change at high rotational frequency, which can result in a very elongated shape. The stiffness of the nucleus is found by considering magnitude of its moment of inertia which can be calculated by substituting the experimental energies into equation 1.4. The results shows the effective moment of inertia is about one third of that obtained if the nucleus is assumed to be a rigid body at a low spin. This is because of the pairing interaction effects, which make the nucleus behave like a superfluid. The nucleus is somewhere between these two extremes. It has been experimentally observed that the nucleus does not rotate like a rigid body, however part of its nucleons are participating in the collective rotation of the nucleus.

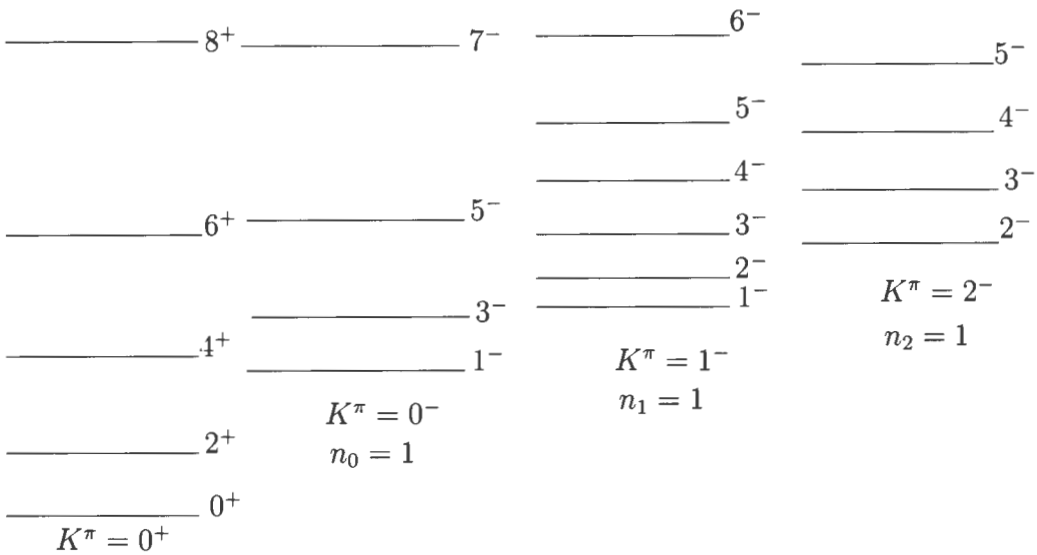

Figure 1.8: Vibrational bands built on octupole vibrational states in quadrupole-deformed nuclei. The bands are labeled in terms of K angular momentum projection on symmetry axis and n_k is the harmonic oscillator quantum numbers [Eis87].

1.4.2 Octupole vibrations

The octupole vibration has a multipolarity $\lambda = 3$. It has parity $\pi = (-1)^\lambda$ band, which means the parity is negative for $I = 1, 2, 3, 4, \ldots$. The excitation energy associated with a nuclear octupole deformation is typically larger than the energy associated with quadrupole deformation. A typical band structure is shown in figure 1.8. Only the ground state band and the bands built up on the one-octupole phonon states of $K = 0, 1, 2$ are drawn. These bands have been observed for real nuclei [Eis87].

1.4.3 Quadrupole vibrations

Quadrupole vibrations in prolate deformed nuclei are of two kinds: β and γ vibrations. In β vibrations the deformation parameter β oscillates about a mean value β_0. Beta vibrations produce motion in the α_{20} coordinates ($\gamma = 0$). The nucleus preserves its cylindrical symmetry. The distance along the x and y direction of the body fixed axes are always equal to each other, but the distance along the z axis (long axis) is changing with respect to time. Such vibrations have states with projection of total angular momentum $K = 0$, only even spins can occur and the parity is positive, $I^\pi = 0^+, 2^+, 4^+, \ldots$. Gamma vibrations do not posses cylindrical symmetry. The vibration is along the x and y axes. These vibrations

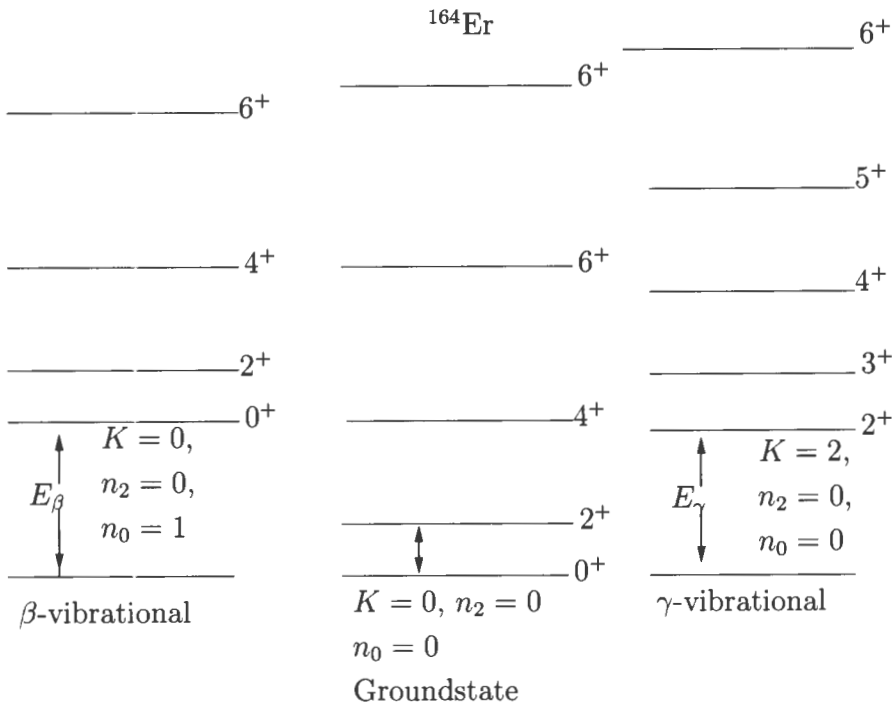

Figure 1.9: Band structure for a even-even nucleus ^{164}Er showing the $K = 0$, ground and $K = 2$ quadrupole vibrational bands, where K is the angular momentum projection on symmetry axis and n_k is the harmonic oscillator quantum numbers.

carry two units of angular momentum having states with $K = 2$, odd and even spins and parities $I^\pi = 2^+, 3^+, 4^+, \ldots$. The energy of the phonon excitation is typically 1 MeV, while the rotational spacing is much smaller.

The low-energy structure of the even-even nucleus ^{164}Er [Eis87] is shown in figure 1.9. The bands are labeled with a set of xed quantum numbers K, n_2, n_0. The rotational bands show the characteristic $I(I+1)$ spacing. The β-vibrational band lies at energy $E_\beta = \hbar\omega_\beta$, where ω_β is the angular frequency for the β vibrations and for γ vibrations the energy lies at $E_\gamma = \hbar\omega_\gamma$, where ω_γ is the angular frequency for the γ vibrations.

1.5 Tetrahedral rotational bands

As we know, the tetrahedral deformation has the octupole character, $\alpha_{32} \neq 0$, with a multipolarity $\lambda = 3$, the rotational band has an alternating parity. Figure 1.10, shows the expected tetrahedral rotational bands with odd and even spin and alternating parity. These present a unique signature of the tetrahedral bands that is not present in quadrupole rotational

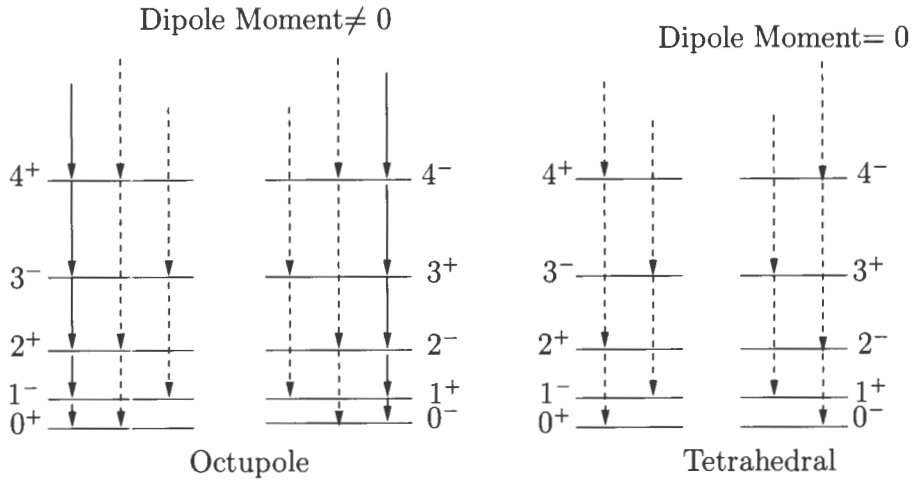

Figure 1.10: Schematic illustration of the rotational bands associated with the tetrahedral shapes (right) as well as those associated with the axially-symmetric octupole shapes (left).

bands. It is also seen that the tetrahedral rotational bands are similar to the bands of an octupole deformed nucleus. The intra-band $E2$-transitions are expected to be weak because of the relatively small values of the quadrupole moments. The dipole inter-band transition probabilities from the bands to the ground-state bands are expected to be larger compared to the intra-band $E2$ transition probabilities, especially at the bottom of a tetrahedral band. Experimentally the results are expected to contain only the intra-band $E1$ transitions due to the side-feeding of the tetrahedral bands and weak or no $E2$ transition at all [Dud06].

1.6 Location of tetrahedral bands

Before this experiment was proposed, tetrahedral shapes were predicted to lie relatively low in excitation energy in ^{160}Yb by Dudek *et al.* [Dud02], at excitations energies of about 1.4 MeV above the ground state. This energy 1.4 MeV was low in comparison with the predictions for the other mass regions. The signature of tetrahedral nuclear shape is shown in figure 1.10. It was theoretically predicted to be bands with degenerate levels and alternating parity. During the data analysis of this work, papers have been published, claiming that the signature of a tetrahedral band is one negative parity and a strong $E1$ transition to the ground state band. These bands were formally considered to be octupole vibrational bands and the excitation energy is some hundreds keV in ^{156}Gd and ^{160}Yb nuclei, Dudek *et al.* [Dud06, Dud07].

Figure 1.11 illustrates the expected position of the non-yrast states of the nucleus that has

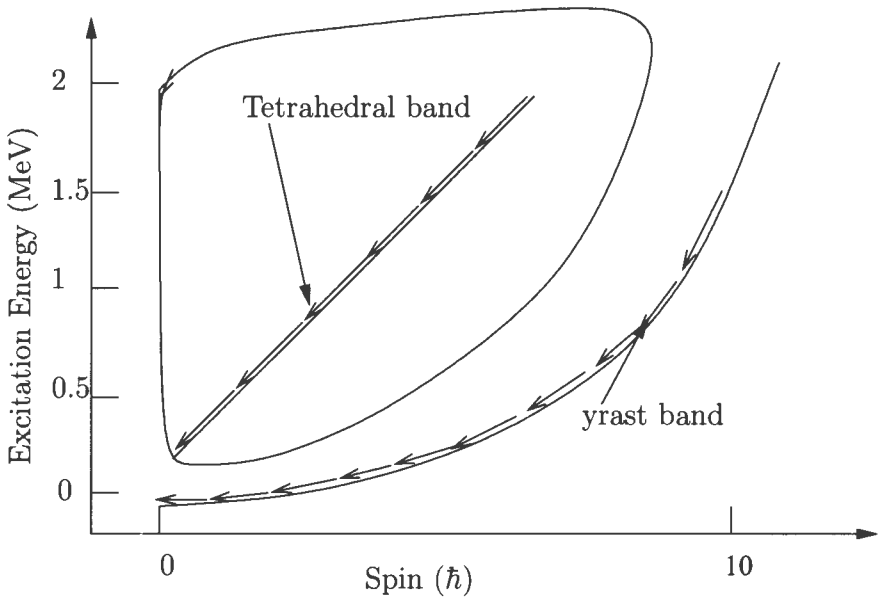

Figure 1.11: This sketch illustrates the expected position of tetrahedral band.

tetrahedral symmetry. Non-yrast states are the states having the higher excitation energy for a given spin above the ground state band. The schematic diagram shows that the tetrahedral bands can lie low in excitation energy above the ground state, but remain well above the yrast line.

The tetrahedral bands might be located away from the yrast line. Energy of the tetrahedral bands will probably follow the $E = AI(I+1)$ trend, where $A = \frac{\hbar^2}{2\mathcal{I}}$. The calculations were first interpreted to say that the energy of the band E_0 could be high [Dud02]. But because A is not known, there is then the possibility that it could be small and that is why the tetrahedral bands had not been seen.

In the spin-energy region where we expect to observe the tetrahedral states, we also expect to observe the vibrational bands. It is possible that the tetrahedral bands will be competing with quadrupole and octupole vibrational bands. Because the tetrahedral deformed nucleus has a strong octupole character, the tetrahedral bands could then possibly be confused with octupole bands.

Chapter 2

Methods of populating low spin states

Low spin states in nuclei can be populated in several methods: Coulomb excitation, transfer reactions, neutron scattering, neutron absorption, β^+-decay, and (HI,xn) reaction. Since the nucleus of interest ^{160}Yb is far from stability, the best way to reach it is to populate through heavy-ion nuclear reactions or β-decay of ^{160}Lu measurements. Beta-decay measurements was chosen in place of in-beam γ measurements because this experiment had been performed already at the iThemba LABS cyclotron [Bar05, Mal06] and is discussion in section 2.1.2.

2.1 Formation of compound nucleus in heavy-ion reactions

Heavy-ion nuclear reactions are ones in which a heavy ion (HI) beam, for example a projectile with $A > 4$, is used. The impact parameter b determines which process can occur in heavy-ion reactions: elastic scattering or direct reactions, compound nucleus formation, dissipative collision and elastic (Rutherford) scattering as indicated in figure 2.1. The angular momentum L is proportional to the impact parameter b and is given by:

$$L = pb = b\sqrt{2mE}, \tag{2.1}$$

where $p = mv$ is the linear momentum, m is the reduced mass of the projectile-target system, and v is the velocity of the particles. Because all the particles (projectile and the target nucleus) involved in the reaction are positively charged, they will repel each other. When the projectile and the target nuclei are close enough the strong attractive nuclear

forces comes to play a role of bringing them together, but at a large separation the Coulomb repulsion is not negligible and has an important influence on the probability of two nuclei coming into contact and undergoing a reaction. The Coulomb potential is given by:

$$V_{cb}(R) = \frac{1}{4\pi\epsilon_0}\frac{Z_b Z_t e^2}{R} \tag{2.2}$$

where $Z_b e$ and $Z_t e$ are the charge of the projectile and the target nucleus, respectively, ϵ_0 is the permittivity of free space, and R is the distance between the projectile and the target nucleus in the interaction. When the impact parameter b is large the peripheral collisions can also occur and the highly excited compound nucleus is formed with high angular momentum. If the energy is not higher than the barrier, the Coulomb effects will dominate, which means the Rutherford elastic scattering or Coulomb excitation may occur. In this reaction the incoming particle and the outgoing particles are the same, but the direction of the wave propagation is changed. The target nucleus may be in its ground state or internally excited. When the beam energy is higher than the barrier, and the impact parameter b is small, a central collision between the projectile and the target nucleus can occur and resulting in an excited compound nucleus will have relatively low angular momentum.

Once the two nuclei fuse together their separate identity is lost. Energy of the beam is converted to excitation energy of the compound system and subsequently shared between the constituent nucleons of the nucleus. The excitation energy E^* is well defined for each reaction and is given by:

$$E^* = \frac{A_t}{A_b + A_t}E_{lab} + Q, \tag{2.3}$$

where A_b and A_t are the mass number of the projectile and the target nucleus respectively and Q is the corresponding Q value. Because we do not have the control of b, to achieve the desired angular momentum in the compound system the mass and energy of the heavy-ion beam must selected as indicated by equation 2.1. The compound nucleus can take all of the possible values of the angular momentum up to a maximum because the impact parameter is random. Semi-clasically, what we get from the reaction is the angular momentum distribution shown in the figure 2.2 (right). Larger L values (that is larger b) have larger cross sections, as the area of the ring of width db is proportional to b. Lets consider the nucleus as a black disk [Bla52], and all the particles that strike are absorbed. The left sketch is the nucleus with the shaded ring given by:

$$d\sigma = 2\pi b db. \tag{2.4}$$

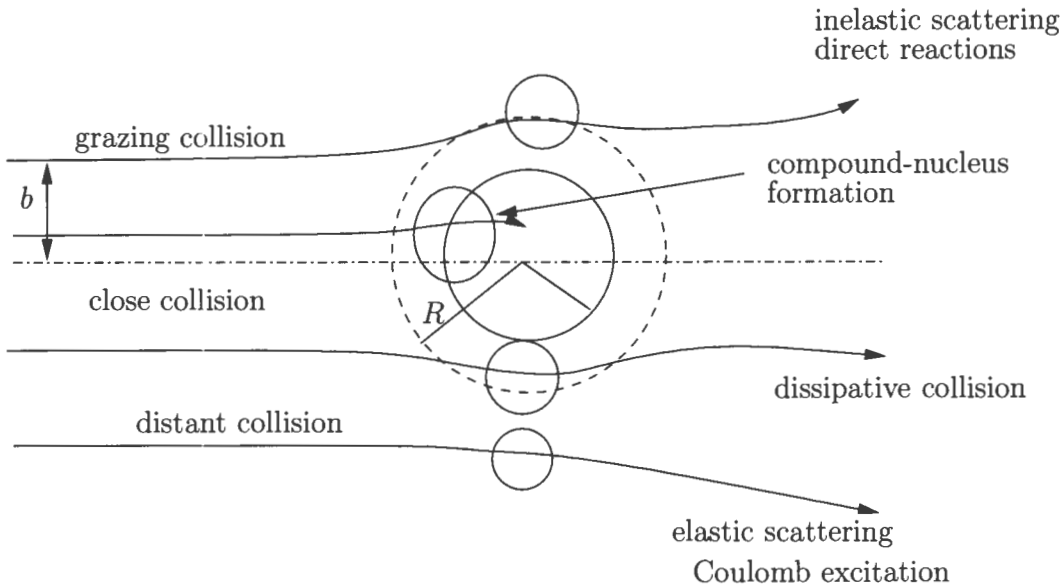

Figure 2.1: The illustration of different types of heavy-ion nuclear reactions.

After integration, the cross-section for nuclear reactions becomes:

$$\sigma = \pi R^2, \tag{2.5}$$

where R is the distance from centre of the target nucleus to the projectile. In reality, the Coulomb repulsion force between the projectile and the target nucleus exist. When the energy of the beam is less than the Coulomb barrier, the particles will be reflected back, and in this case penetration is classically forbidden [Sat80]. However, barrier penetration can occur because of quantum mechanical tunnelling [Bla52]. Here, we confine ourselves to a semiclassical treatment. To perform the calculations for the fusion cross-section, we take equation 2.1 and differentiate b with respect to L to obtain:

$$\frac{db}{dL} = \frac{1}{\sqrt{2mE}}. \tag{2.6}$$

Substituting b and db from equation 2.1 and 2.6 respectively in equation 2.4 then we obtain:

$$d\sigma' = 2\pi \frac{L}{\sqrt{2mE}} \frac{dL}{\sqrt{2mE}} = \frac{\pi}{mE} L dL. \tag{2.7}$$

Integrating equation 2.7

$$\int_0^{\sigma} d\sigma' = \int_0^{L_{max}} \frac{\pi}{mE} L dL = \frac{\pi}{2mE} L_{max}^2, \tag{2.8}$$

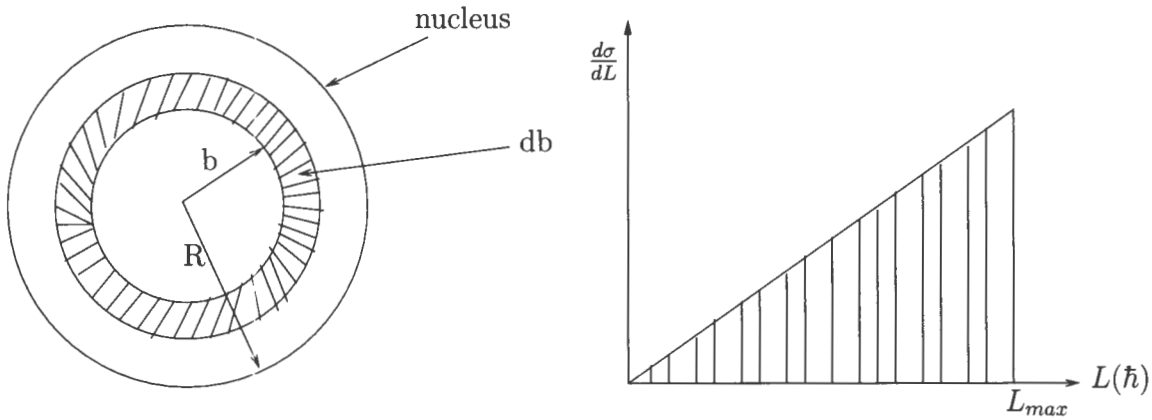

Figure 2.2: The schematic view of the nucleus cross-section area (left) and the sketch of cross-section as function of angular momentum of the nucleus (right).

where $L^2_{max} = \ell_{max}(\ell_{max}+1)\hbar^2$. If the maximum angular momentum is defined to be that for which the total barrier height is equal to E, then:

$$E = V_C + \frac{\ell_{max}(\ell_{max}+1)\hbar^2}{2mR^2}, \tag{2.9}$$

where the first term is the Coulomb potential (Coulomb barrier) and the second one is the "centrifugal" potential (centrifugal barrier). Both effects do not allow the particle to enter or leave the nucleus. Semi-classically, all the partial waves up to L_{max} will fuse. If we take $\ell_{max}(\ell_{max}+1)\hbar^2$ from equation 2.9 and substitute into L^2_{max} in equation 2.8 then the fusion cross-section area as a function of energy will be:

$$\sigma_{fus}(E) = \pi R^2 \left(1 - \frac{V_C}{E}\right), \tag{2.10}$$

where R is the position of the barrier, E is the beam energy and V_C is the barrier height.

2.1.1 The de-excitation of the compound nucleus

Within 10^{-20} s the highly excited compound nucleus cools down by emitting a few neutrons and sometimes an additional proton or alpha particles, as seen in figure 2.3. Once cooled below the particle separation energy of a neutron (about 8 MeV) above the yrast line, the system cools down further by the emission of a few high energy "statistical" γ rays. The yrast line is the states of lowest energy for a given spin. On the average very little angular momentum (1-2$\hbar$) and high excitation energy is removed from the compound nucleus during

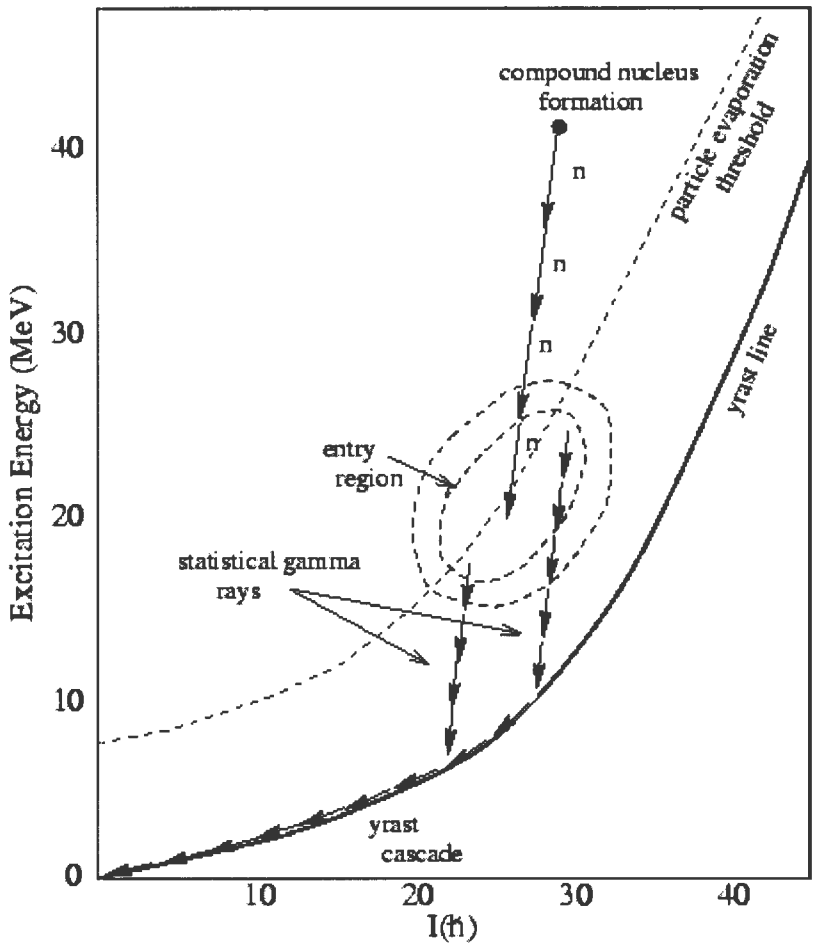

Figure 2.3: The fusion evaporation reaction diagram illustrating how the compound nucleus de-excites to ground state [Nil95].

this rapid cooling period. When the compound nucleus evaporates particles such as protons or alpha particles, it results in the population of several channels, which depend on the charge to mass ratio.

2.1.2 Population of low spin states using in-beam γ spectroscopy

In the in-beam γ measurements performed at iThemba LABS the nucleus ^{160}Yb was created using the heavy-ion fusion evaporation reaction ^{147}Sm(^{16}O,3n)^{160}Yb by Maliage [Mal06]. The energy of the heavy-ion beam was 73 MeV, just enough to overcome the Coulomb barrier between the two nuclei. A thick target was used in order to minimize the residual nucleus from recoiling out of the target. Gamma rays emitted from the residual nucleus were detected

by the AFRODITE HpGe detector array. Figure 2.4 shows the cross-section calculations done using the program PACE [Hil80]. The beam energy of 73 MeV loses sufficient energy while hitting and passing through the target that the entire reaction cross-section integrated down to the Coulomb barrier, thereby enhancing the population of the low spin states. This heavy-ion (Oxygen,3n) reaction was successful in populating the low spin states (the level scheme is shown in figure 2.5), but the tetrahedral states were evidently not populated. The results obtained from this experiment assured us that AFRODITE instruments are efficient in measuring γ rays with the high resolution and are discussed in chapter 5 together with what we have observed previously and recently in β-decay measurements.

2.2 Beta decay of the nucleus

Beta-decay measurements are also one of the best tools we can use to populate the low spin states in the nucleus. Beta-decay is a transition between two nuclei of the same mass number $A = N + Z$ that change both the nuclear charge number Z and neutron number N. The transformation is mediated by the weak nuclear force, which changes a neutron to a proton or vice versa. The are two types of β decay, β^+ and β^- decay. In β^+ decay, the unstable nuclei with proton excess decay through the conversion:

$$\mathrm{p} \rightarrow \mathrm{n} + e^+ + \nu_e, \tag{2.11}$$

where e^+ and ν_e are the positron and electron neutrino, respectively. Beta plus decay is likely to occur whenever the following relationship between the masses $M(A,Z)$ and $M(A,Z-1)$ of the parent and the daughter atoms respectively are satisfied: $M(A,Z) > M(A,Z-1)+2me$. The energy released as kinetic energy is then $K = (M(A,Z) - M(A-Z+1))c^2 - 2m_e c^2$.

In β^--decay, the unstable nuclei with more neutrons decay through the conversion:

$$\mathrm{n} \rightarrow \mathrm{p} + e^- + \overline{\nu}_e \tag{2.12}$$

where e^- is the electron and $\overline{\nu}_e$ is the antineutrino emitted from the nucleus. The charge number of the daughter nucleus is one unit larger than that of the parent nucleus. Energetically, β^--decay is possible whenever the mass of the daughter is smaller than the mass of the isobaric parent; $M(A,Z) > M(A,Z+1)$, since neutrino is massless. The energy released as kinetic energy is then $K = (M(A,Z) - M(A-Z+1))c^2$. Typically, the decay continues from the ground state of the initial nucleus to the ground state of the final nucleus, although

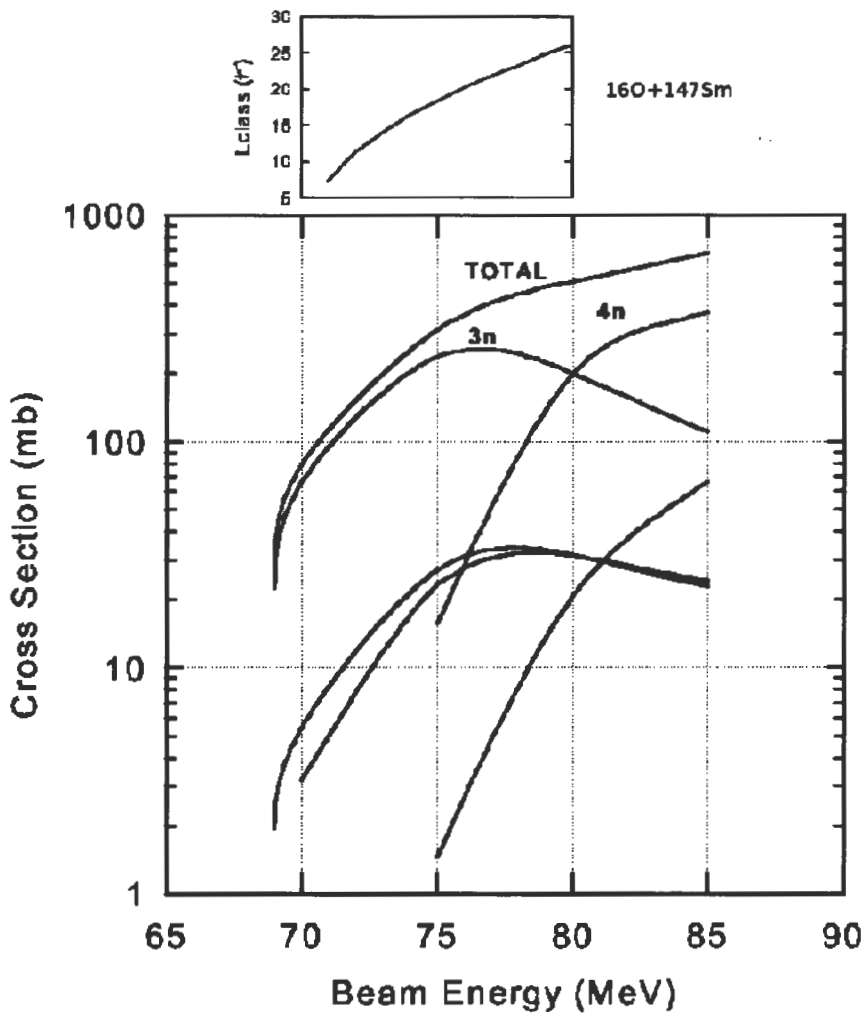

Figure 2.4: The reaction cross-section calculations for in-beam γ spectroscopy experiment [Mal06].

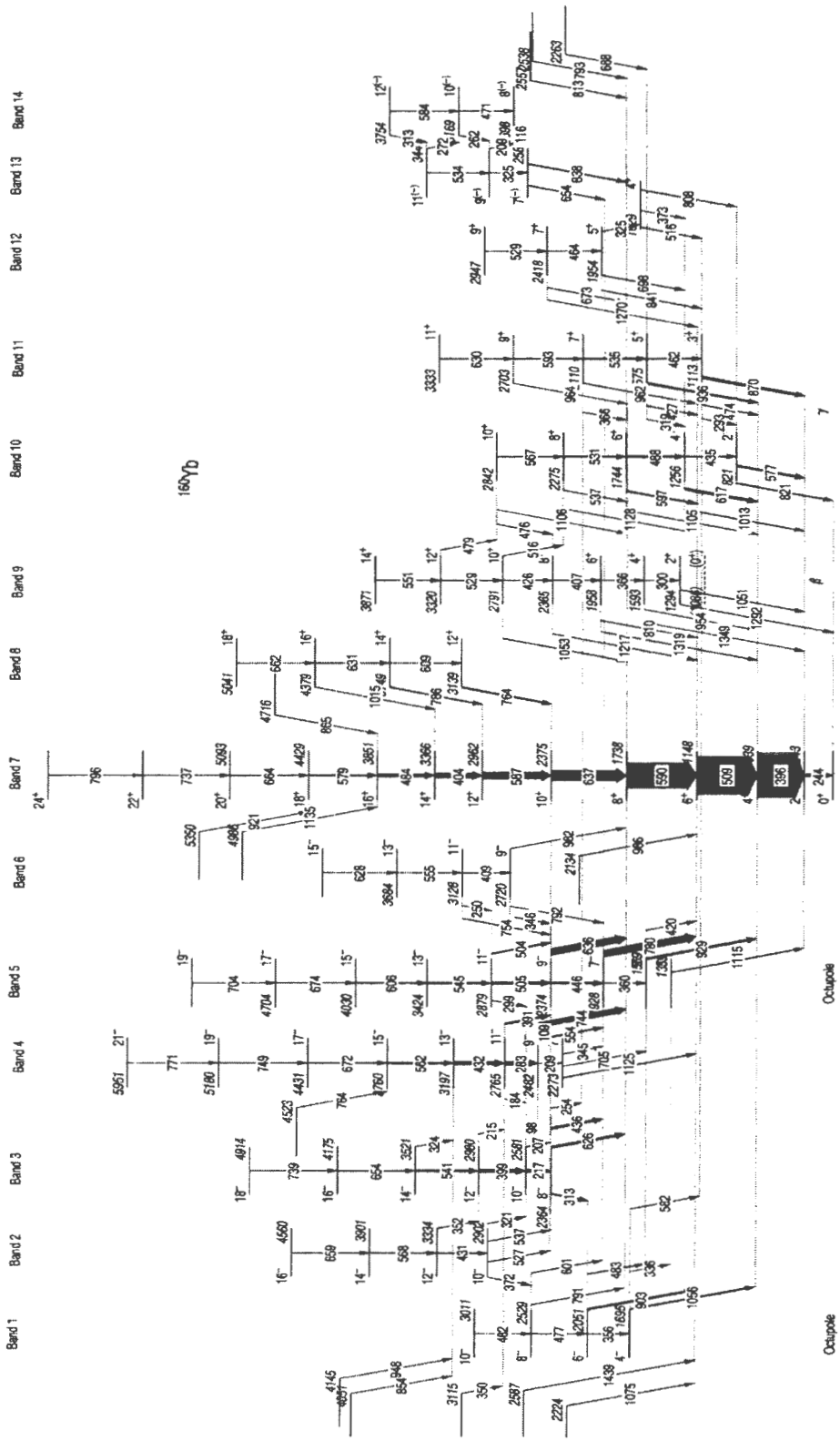

Figure 2.5: Level scheme of ^{160}Yb from in-beam γ-ray spectroscopy using AFRODITE array [Mal06].

the decay into excited states in some cases is also energetically possible.

2.2.1 Electron capture (EC)

In electron capture, the nucleus with excess protons captures an electron and a proton is changed into a neutron. This happens because the nucleus does not have sufficient energy to emit a positron. Electron capture is caused by the weak interaction and it usually competes with the β^+ decay, when both decay modes are possible. The decays rates depend on the overlap of the atomic electron's wave function with that of the nucleus, a phase-space factor, and the matrix element M. However, the operation of the weak interaction of the nucleus is the same for EC as for β^+ emission. In this case, an electron in the orbital electron shell K or L can be captured. Because the K shell electron has a greater chance of being close to the nucleus than the L shells, the electron in the atomic K shell of an atom is most likely to be captured. The capture is possible because the $l = 0$ radial wave function of the K-shell electron peaks at $r = 0$, which occurs inside the nucleus. The size of the K-electron orbit varies roughly inversely with the atomic number Z. Therefore, the volume it occupies will scale approximately as $1/Z^3$, and its overlap with the nucleus as Z^3. This implies that the EC increases fast with Z, because positron emission is inhibited by the Coulomb barrier for positive particles near the nucleus and decreases with Z. The ratio of EC to β^+ decay increases with decreasing E_0. Energy released in EC is greater than that for β^+ emission by $2mc^2$. If the energy difference between the parent and the daughter is less than 1.002 MeV, positron emission is forbidden and electron capture is the allowed decay mode. In EC, the mass of an electron is converted into energy, whereas in β^+ emission energy is required to create the positron.

2.2.2 Selection rules

The selection rules of β-decay give us insight on the states which are mostly likely to be populated, i.e low spin states. We consider the β-transition between two nuclear states of well defined angular momentum with the emission of an electron and a neutrino. In this transition, the total angular momentum and the parity of the states must be conserved. The total angular momentum is the sum of the orbital angular momentum and intrinsic contributions. In beta decay we have allowed and forbidden decays. In the allowed decays, the orbital angular momentum that electron and neutrino carry is zero and the change in the angular momentum of the nucleus must come from the intrinsic spin of these particles. Since

the electron and neutrino are fermions with spin $1/2\hbar$, the are two cases to consider; the transitions with combined spins to give total $S = 0$ or $S = 1$. Total $S = 0$ and $S = 1$ mean that the two spins are antiparallel and parallel respectively. Each combination corresponds to different type of transitions. The transitions with $S = 0$ and $\ell = 0$ are known as the Fermi transitions. There is no change in the nuclear spins: $\Delta I = |I_i - I_f| = 0$. The total $S = 1$ transitions are known as Gamow-Teller transitions in the allowed decays, the leptons carry one unit of total angular momentum. In this case the initial spin I_i and final spin I_f must couple through a vector of length 1, i.e $I_i = I_f + 1$ and is likely to occur if $\Delta I = 0$ or 1. If the orbital angular momentum $\ell = 0$ then the parities of the initial and the final state must be the same, since the parity associated with the orbital angular momentum is $(-1)^\ell$. For allowed β decays the selection rules are:

$$\Delta I = 0, 1 \quad \Delta\pi = \text{no}$$

The forbidden decays are less likely to occur than allowed decays, because they have longer half-lives. The only chance that this decay can occur is when the matrix elements of an allowed decays happen to disappear. The forbidden decays violate the selection rule for allowed decays because it allows the parity of the initial and the final state to be different. The electron and neutrino must be emitted with an odd value of the orbital angular momentum relative to the nucleus. We consider the first forbidden decays with $\ell = 1$. In forbidden decays, like the allowed decays there are Fermi and Gamow-Teller types of transitions. The Fermi types have electron and neutrino spins opposite $S = 0$, and Gamow-Teller types have spins parallel $S = 1$. For Fermi types, the coupling of $S = 0$ with $\ell = 1$ gives total angular momentum of one unit carried by the β transition, i.e $\Delta I = 0$ or 1. In the Gamow-Teller decays, $S = 1$ couples with $\ell = 1$ to obtain 0, 1, or 2 units of angular momentum, i.e $\Delta I = 0$, 1, or 2. For first forbidden decays $\ell = 1$, the selection rules are:

$$\Delta I = 0, 1, 2 \quad \Delta\pi = \text{yes.}$$

The transitions with $\ell = 2$ are known as second forbidden decays. When we couple $S = 0$ or 1 with $\ell = 2$, we can in principle change the nuclear spin by an amount from $\Delta I = 1$ to $\Delta I = 3$. The allowed selection rules include $\Delta I = 0$ and 1. For second forbidden decays, the selection rules are:

$$\Delta I = 2, 3 \quad \Delta\pi = \text{no}$$

2.2.3 Population of low spin states using β-decay of ^{160}Lu

In this work we review the previous β-decay experiments in order to have a reference of the results we are intending to obtain for the same nucleus. Two β-decay experiments have been devoted to the study of γ rays from β-decay of ^{160}Lu into ^{160}Yb. The first experiment to populate the ^{160}Yb was performed by Garret *et al.* [Gar82]. The parent nucleus ^{160}Lu was created in the ^{151}Eu(^{16}O,7n)^{160}Lu reaction. The obtained γ rays were assigned to ^{160}Yb from the decay of ^{160}Lu on the basis of the measured excitation function in coincidence with Yb K X-rays. The level scheme, shown in figure 2.6 was built from the data obtained. The γ-ray transitions are labeled by the spins I and excitation energy on the left side of the level scheme. In the level scheme it is clear that they were successful in populating the low spin states of ^{160}Yb. The second experiment to create the radioactive ^{160}Lu source was performed by Auer *et al.* [Aue84] using the ^{144}Sm(^{19}F,3n) reaction at a beam energy of 85 MeV. Gamma rays were assigned to the level scheme of ^{160}Yb on the basis of their lifetimes, γ-X-ray and γ-γ coincidence measurements [Aue84]. The most recent and comprehensive β-decay level scheme is shown in figure 2.7. The states from which ^{160}Lu β-decays have been reported by Auer *et al.* [Aue84], two β-decaying states in ^{160}Lu with half-lives of 40(1) s and 36.2(3) s and unknown spin and parity. They suggested that some of the state in ^{160}Yb are populated from the state with a longer lifetimes. The low spin states of ^{160}Yb seem to have been populated from the spin $I < 5$ of the ground state of ^{160}Lu. We proposed to repeat the measurements because the enhanced efficiency of the AFRODITE Ge clover detector may allow us to observe the high energy γ rays which they might not have seen. The results of these two β-decay experiments are also discussed in chapter 5.

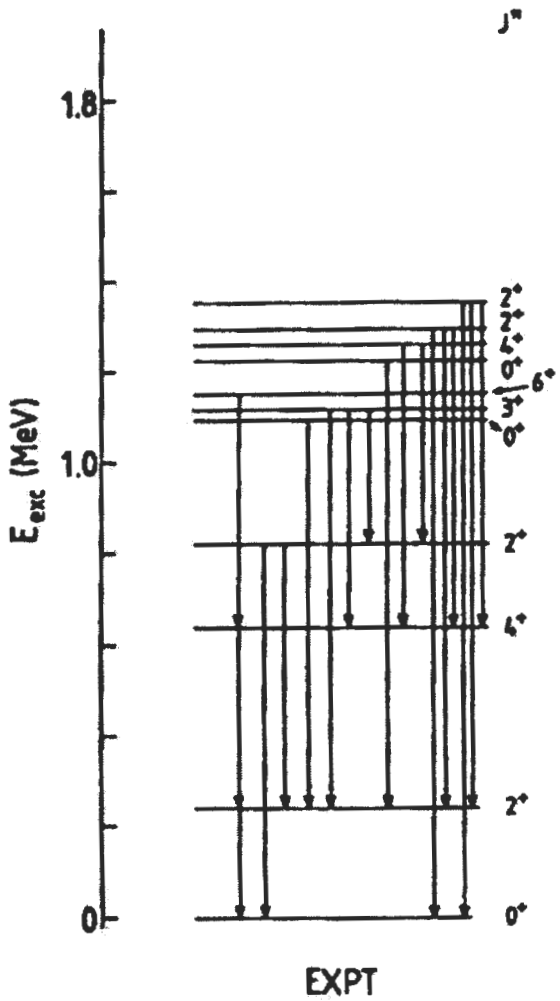

Figure 2.6: The first β-decay measurement of ^{160}Yb [Gar82].

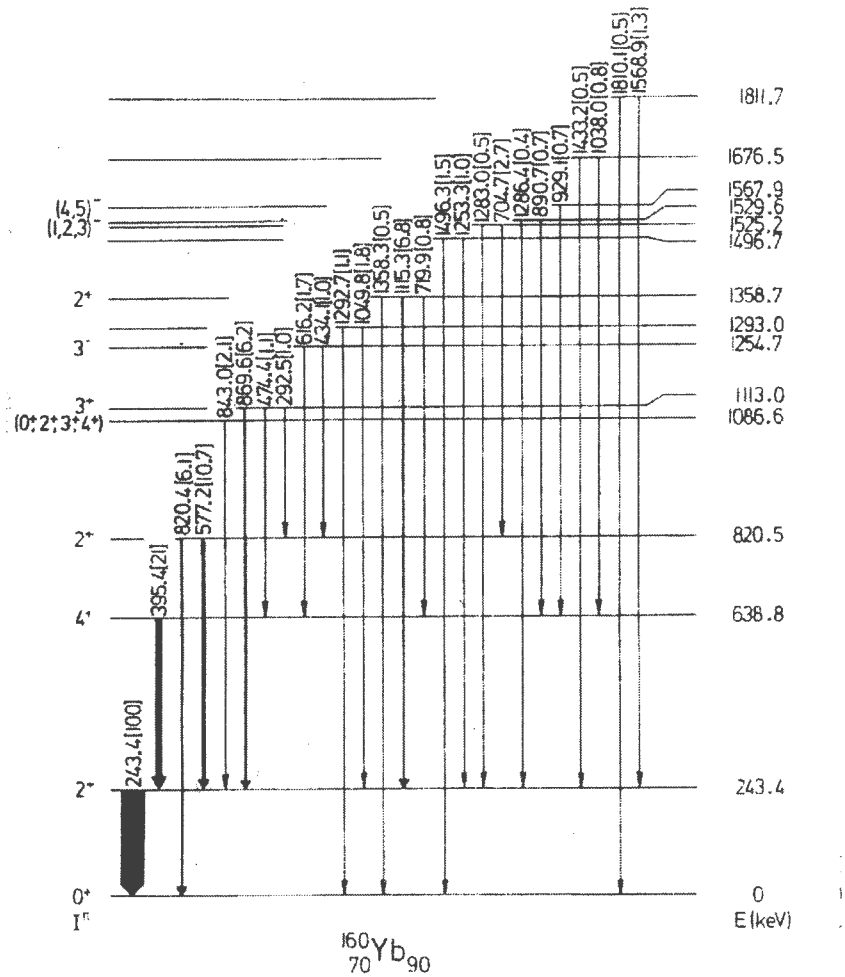

Figure 2.7: The β-decay level scheme of ^{160}Yb [Aue84].

Chapter 3

Experimental procedure

The radioactive nucleus ^{160}Lu was created using the ^{144}Sm(^{19}F,3n) reaction at the AFRODITE vault. The iThemba LABS Separated Sector Cyclotron accelerator provided an 85 MeV ^{19}F beam. This energy was enough to overcome the Coulomb barrier between the projectile and the target nucleus. The AFRODITE detector array consisted of 8 Compton-suppressed segmented Clover HpGe detectors and 3 low energy photon spectrometers (LEPS) in close geometry was used to detect γ rays of high and low energy.

3.1 Reaction selection

To selectively populate the nucleus ^{160}Lu we needed a reaction that minimizes the population of neighbouring nuclei, as their population could complicate the identification of the weak transitions in ^{160}Yb. Using the program PACE (Projection Angular momentum Coupled Evaporation Monte-Carlo code) [Hil80], the optimum reaction was calculated to be ^{144}Sm(^{19}F,3n)^{160}Lu at 85 MeV. The reaction cross-section calculations presented in figure 3.1 show that at the beam energy of 85 MeV the reaction gives the best yield the nucleus of interest as compared to other high beam energy reactions. For this experiment we selected a thick target because we are interested in high energy γ rays at low spin. As the beam passes through the target it will lose energy, effectively integrating the area under the ^{160}Lu curve from the energy of 85 MeV down to the Coulomb barrier. This enhance the population of the low spin states. The target was thick enough to stop the recoiling ^{160}Lu nuclei so that their subsequent decays can be detected by the HpGe detectors in the detection area. The target was 3.4 mg/cm^2 thick and 88.4% enriched ^{144}Sm. It is durable and offers the option of performing lifetime measurements as we intended to do to identify the lines of ^{160}Yb.

3.2 Techniques employed to populate ^{160}Yb

As was discussed earlier, in section 2.1.1, the compound nucleus de-excites by emitting prompt radiation before it reaches ground state and β-decays. This radiation are γ rays emitted from ^{160}Lu and are not of interest. We had to use a technique to minimize this radiation and focus on observing the γ-rays from the excited states of ^{160}Yb after β-decay. Given the two states of ^{160}Lu with half-life of 36 and 40 s, we decided that the target will be irradiated for 45 s inside the target chamber after which the beam was switched OFF for 225 s to do the measurements. We used a beam chopper which was installed at the ion source. The beam chopper chopped the beam continuously, 45 s ON and 225 s OFF. The nucleus ^{160}Lu has two states of 36 and 40 s half-life. The beam was OFF for 5 half-lives to give accurate half-life measurements, at the expense of higher statistics.

During this 225 s OFF beam period, we expected to measure γ rays that follow β^+ decay i.e a singles γ rays or coincident γ rays. The focus was to identify the γ-ray transitions from ^{160}Yb in this data. In singles γ ray measurements to identify if this radiation came from ^{160}Yb, we measured the half-life to see if it is the same as the half-life of the parent nucleus. In coincidence measurements to assign γ rays to ^{160}Yb we required the two radiations to come close enough together in time to originate from the same nucleus. This means that the time interval between the emission of two radiations from the same nucleus should be negligibly short (i.e < 150 ns).

3.3 Decay of radioactive nuclei

To understand the decay of the radioactive nucleus ^{160}Lu we need to recall the radioactive law. We know that any decay transition is characterised by a lifetime. The probability that the nucleus will decay in the time interval dt is λdt, where λ is the decay constant. The probability is independent of the time t. Suppose we have $N(t)$ nuclei present in a particular state at a time t. In a time interval dt a number $N(t)\lambda dt$ will decay. Since the number of nuclei is decreasing, the change in the number $dN(t)$ will be negative.

$$dN(t) = -\lambda N(t)dt \tag{3.1}$$

After integration, the above equation gives the exponential decay law:

$$N(t) = N_0 \exp(-\lambda t) \tag{3.2}$$

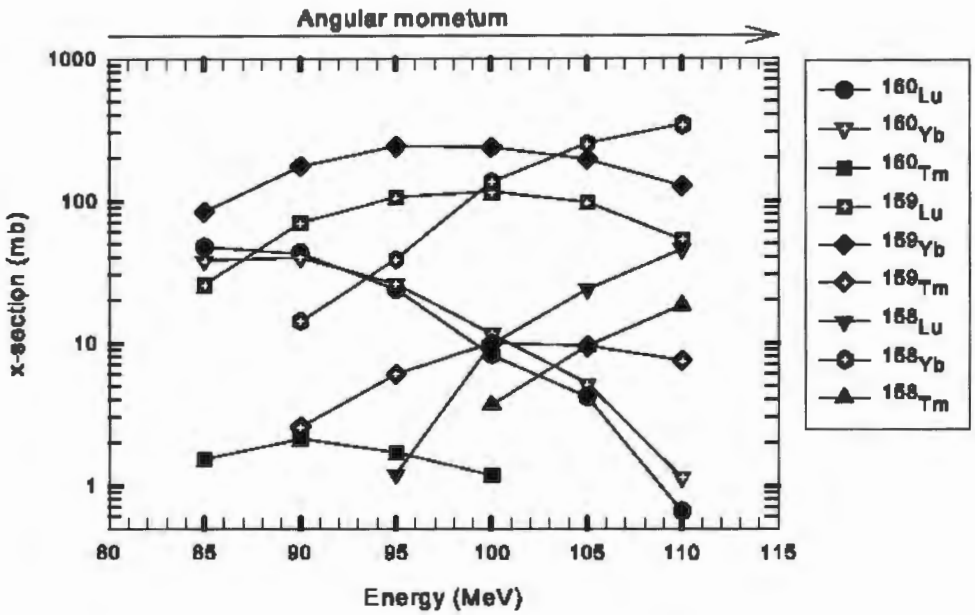

Figure 3.1: The calculated cross section reaction for this experiment.

A characteristic of this equation is that at time $t = 0$, $N(t) = N_0$ and that in a time interval T, a fraction $(1 - \exp(-\lambda T))$ will have decayed. So, in short, the number remaining is decreasing exponentially. We define the half-life $T_{1/2}$ as the time interval in which the half of the initial population of the nucleus decays,

$$T_{1/2} = \frac{\ln 2}{\lambda}, \text{ and the meanlife, } \tau = \frac{1}{\lambda}. \tag{3.3}$$

Normally it is difficult to measure the number of nuclei remaining, but it is fairly easy to measure the number decaying because when they decay they emit radiation which can be detected. The number of decays per second is called the activity,

$$A = \lambda N(t) = \frac{dN(t)}{dt}, \tag{3.4}$$

whose unit is the Becquerel and equals the number of decays per second.

3.3.1 Production of radioactive nuclei

Radioactive nuclei were produced during the in-beam period for 45 s. They also decay in this period. The change of the number of original nuclei $dN(t)/dt$ is the balance between the production rate R and the decay activity.

$$\frac{dN(t)}{dt} = R - \lambda N \tag{3.5}$$

We assume that the production rate R is constant. For $N = 0$ at $t = 0$, integrating equation 3.5 yields:

$$N(t) = \frac{R}{\lambda}(1 - \exp^{-\lambda t}) \tag{3.6}$$

The activity A of the target is given as:

$$A(t) = \lambda N = R(1 - \exp^{-\lambda t}) \tag{3.7}$$

This induced activity builds up with time. Thus for large time $t \gg \lambda$, a saturation point is reached in which the rate of production equals the rate of decay $A(t) \simeq$R and the slope $dN(t)/dt \simeq 0$.

3.4 Calculations of the activity of EC or β^+-decay daughters.

The parent nucleus ^{160}Lu has to decay to populate the daughter nucleus ^{160}Yb, which we know is far from stability and this daughter then decays to populate another daughters, and so on, until it reaches a stable state. It was proposed to swap the target every 12 hrs or so to avoid the growth of daughter activity from β-decay. Because of a technical problems the target was not replaced with the fresh one as proposed. We used one target for the whole weekend of beam time. Calculations were performed to understand how the growth of daughter activity from β-decay increases with time. The production of the nucleus ^{160}Lu was periodic, we wanted to find out how many events (production and decay) occurred during each successive beam-off interval. Firstly the calculations of the simplified decay chain shown in figure 3.2 are considered, using the Laplace transforms, where λ_0, λ_1, λ_2, λ_3 and λ_4 are the decay constants. The detailed calculations are as follows; the state $i = 0$ is directly fed

from the reaction and its decay at a time t is given by

$$N_0(t) = N_0(0)\exp(-\lambda t). \tag{3.8}$$

Let us consider the i^{th} state for which,

$$dn_i(t) = \lambda_{i-1}n_{i-1}(t)dt - \lambda_i n_i(t)dt, \tag{3.9}$$

where $\lambda_{i-1}n_{i-1}$ is the number of decays from state $i-1$ to i and $\lambda_i n_i$ is the number of decays from state i. This means that the number of daughter nuclei increases as a results of decays of the parent and decreases as a result of its own decay. Applying the Laplace transform to the differential equation 3.9 we obtain

$$N_i(s) = \frac{\lambda_i - 1}{s+\lambda_i}N_i - 1(s). \tag{3.10}$$

For the case $i = 1$, we have

$$N_1(s) = \frac{\lambda_0}{s+\lambda_i}N_0(s), \tag{3.11}$$

and for $i = 2$

$$N_2(s) = \frac{\lambda_1}{s+\lambda_2}.\frac{\lambda_0}{s+\lambda_1}N_0(s). \tag{3.12}$$

In general

$$N_i(s) = N_0(s)\prod_{j=1}^{i}\left(\frac{\lambda_{i-1}}{s+\lambda_j}\right). \tag{3.13}$$

The Laplace transform of equation 3.8 is given by

$$N_0(s) = N_0(0)\frac{1}{s+\lambda_0}. \tag{3.14}$$

therefore

$$N_i(s) = N_0(0)\prod_{j=0}^{i-1}\lambda_i\sum_{k=0}^{i}\frac{C_{ki}}{s+\lambda_k}, \tag{3.15}$$

where by the cover up rule (Heaviside's Theorem),

$$C_{ji} = \prod_{k=0\ \ k\neq j}^{i}\frac{1}{\lambda_k - \lambda_j}. \tag{3.16}$$

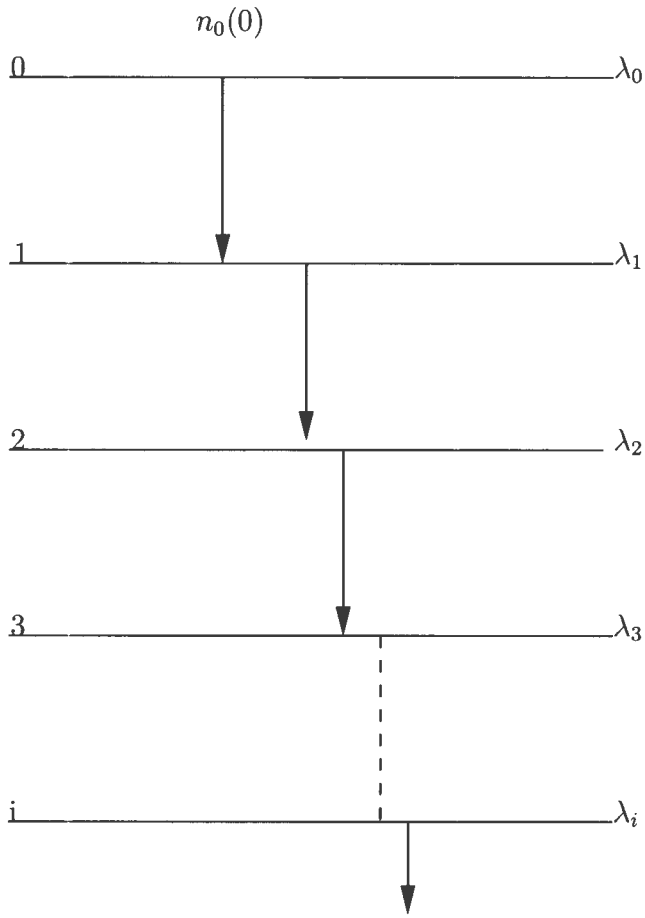

Figure 3.2: Diagram illustrating a general simplified EC and β^+-decay chain.

Then the equation that represent the series of decays (Batemans equation) is:

$$n_i(t) = n_0(0) \prod_{j=0}^{i-1} \lambda_j \sum_{k=0}^{i} C_{ki} \exp(-\lambda_k t). \tag{3.17}$$

The production of ^{160}Lu was in the form of periodic pulses. Figure 3.3 is the schematic diagram of the single pulse drawn in order to simplify the calculations. The equation for that single pulse is given by:

$$f(t) = U(t) - U(t-a) \tag{3.18}$$

where $U(t)$ is the Heaviside's unit step function, defined by:

$$U(t) = \begin{cases} 1 & \text{for} \quad t > 0 \\ 0 & \text{for} \quad t < 0 \end{cases} \tag{3.19}$$

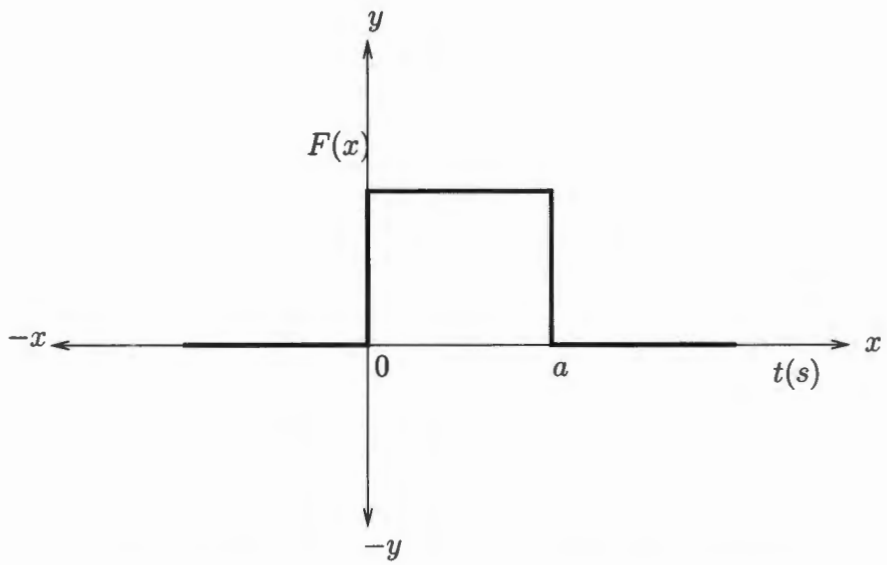

Figure 3.3: Beam pulse series, ON for time $t = a = 45$ s and OFF for time $t = 225$ s.

where t is the time in seconds, and a is the time the beam or pulse is ON.

The Convolution Theorem was used in these calculations to convolute the equation of decay 3.17 with the equation of one beam pulse 3.18 to obtain:

$$N(i,t) = \prod_{j=0}^{i-1} \lambda_j \sum_{k=0}^{i} C_{ki}/\lambda_k \left[1 - e^{-\lambda_k t} - U(t-a)(1 - e^{-\lambda_k (t-a)})\right], \tag{3.20}$$

where

- C_{ki} is the same as C_{ji} given by equation 3.16.
- λ_k is the decay constant ($k = 0, 1, 2, 3 \ldots$), for example for $k = 0$, λ_0 is the decay constant for ^{160}Lu as seen in figure 3.2.

In our case we do not have any parent atoms of ^{160}Lu at a time $t = 0$, i.e $N(i = 1, t = 0) = 0$, and no atoms of the decay products are originally present at $t = 0$, i.e $N(i = 2, t = 0) = N(i = 3, t = 0) = \ldots = 0$.

3.4.1 Simulation of β-decay chain for nuclei with mass number $A = 160$

A code using equation 3.20 to simulate the production and the decay of ^{160}Lu was written (see Appendix A). In this code the decay constant for the parent and the daughters were taken from the decay scheme shown in figure 3.4. To simplify the problem only strong decay transitions were presented and considered in the code. For example, ^{160}Lu has two states that have half-lives of 36 and 40 s, the average half-life of 38 s was used to calculate the decay constant λ. The nucleus ^{160}Yb decays from the ground state with half-life of 4.8 m, this was the value used to calculate the λ in the code. The daughter of ^{160}Yb has two states 74.5 s and 9.4 m (half-lifes), the 9.4 m state of lower spin 1^- was used in the code as it is this state that is fed by the decay of ^{160}Yb. The ground state of ^{160}Er with half-life of 28.58 h decays to ^{160}Ho and this nucleus has two states with half-life of 5.02 h and 25.6 m. In the code the half-life of 5.02 h was used because all intensity passed through this state.

The table of radioactive isotopes is shown in figure 3.5. The blocks which form a diagonal line can be seen starting from the parent nucleus ^{160}Lu decaying through β^+ or EC until reaches the daughter ^{160}Er which is stable. It is taken especially for the β^+-decay of nuclei with mass number $A = 160$. The plot shown in figure 3.6 is when the ^{160}Lu source was produced for 45 s and left to decay over a long period. From the diagram we can see that during the production time some activity formed was decaying, but these activities are not counted since the beam was still ON. During the experiment we had more than one beam pulse, so the code was modified to sum up the production and the decay due to a large number of pulses, as seen in figure 3.7. The beam-off time of 225 s was suitable to measure the γ-rays from the β^+-decay of ^{160}Lu, where in that period almost all of the activity decayed. In the plot it is seen that ^{160}Tm will reach equilibrium after around 20 pulses, which implies that the population of the state is equal to its decay, but ^{160}Er is still increasing. This is because the half-life of ^{160}Er is longer, at 28 hrs. Figure 3.8 is the expanded view of figure 3.7, to emphasize the equilibrium state of ^{160}Lu, ^{160}Yb, and ^{160}Tm.

3.5 AFRODITE (AFRican Omnipurpose Detector for Innovative Techniques and Experiments) array

Gamma rays emitted from excited states of ^{160}Yb after β-decay were detected using the AFRODITE array. This is an array of High purity germanium detectors placed in a frame

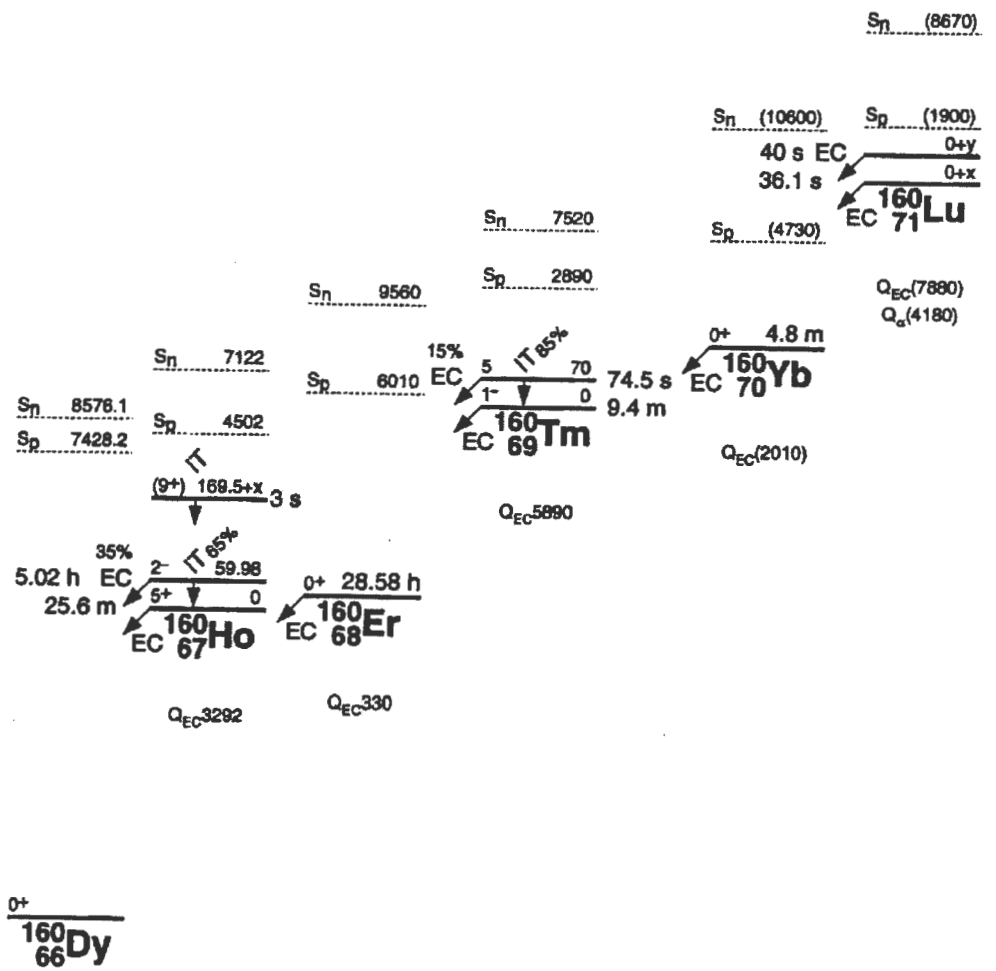

Figure 3.4: The Electron Capture and β^+-decay chain for mass number $A = 160$ [Fir96].

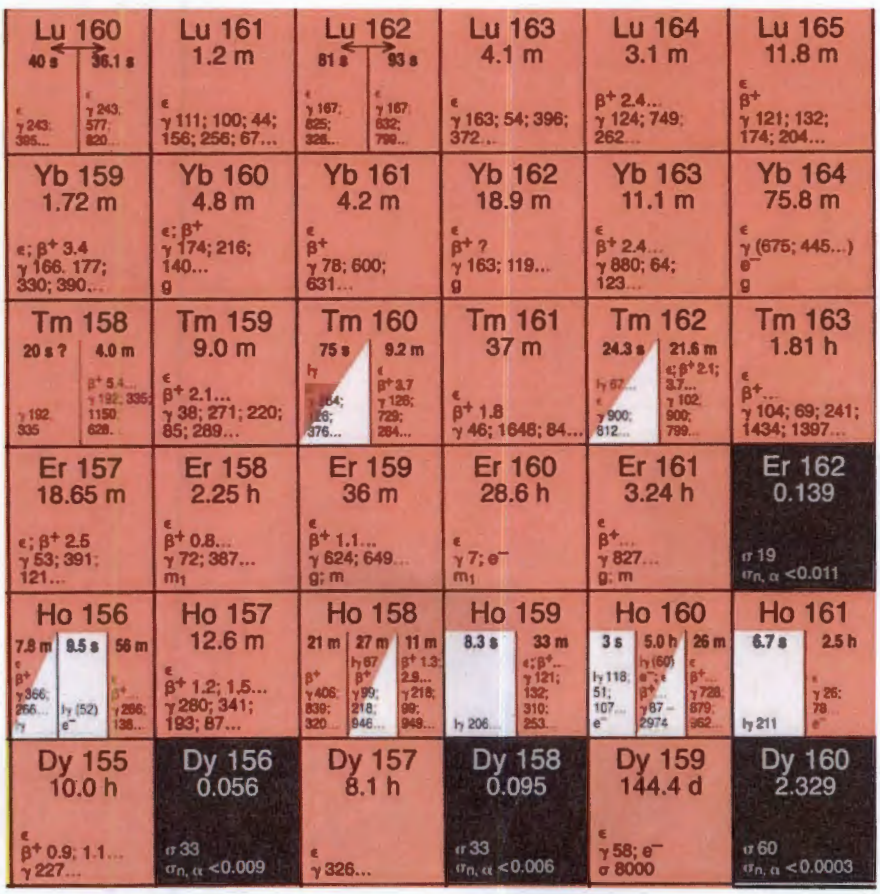

Figure 3.5: The chart of isotopes, captured just for our case for the decay chain of nuclei with mass number $A = 160$. The pink and black shaded box is for radioactive and stable elements respectively [Fir96].

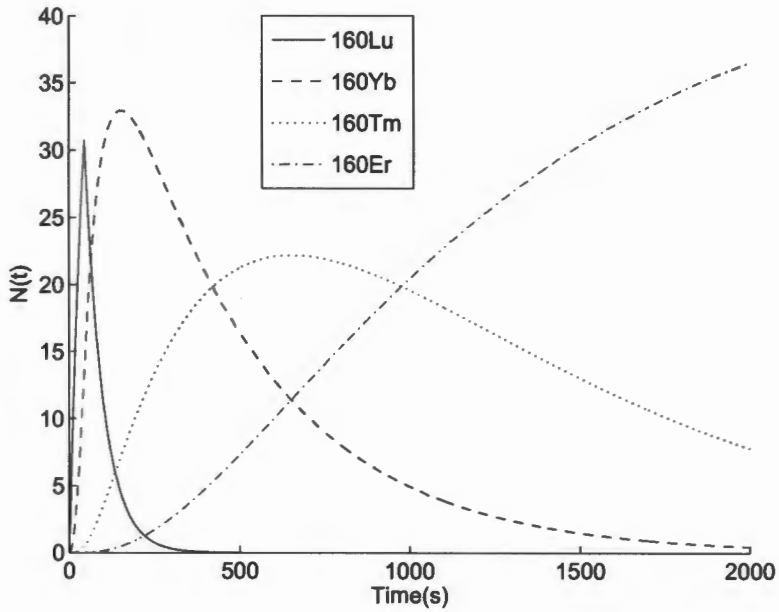

Figure 3.6: Population of ^{160}Lu and its daughters after one beam pulse only.

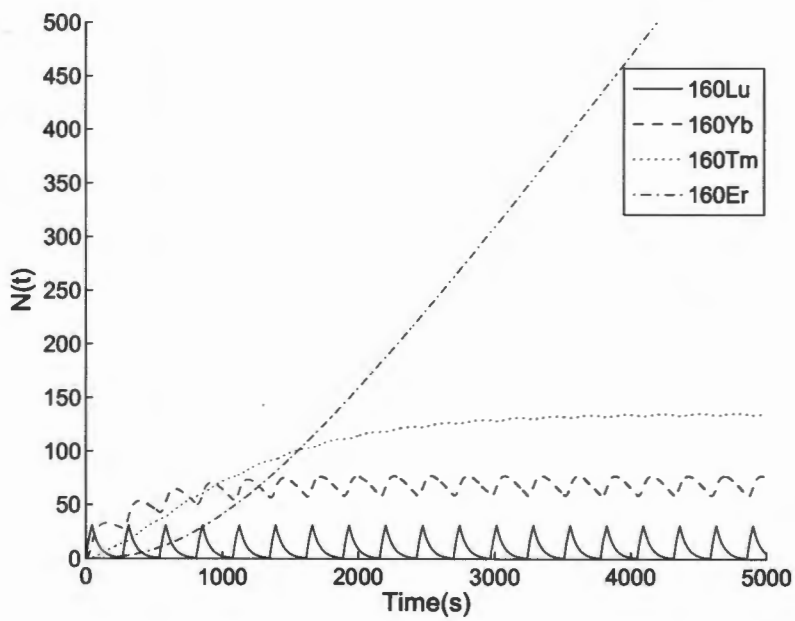

Figure 3.7: A plot of large number of beam pulses showing some of the nuclei reaching equilibrium.

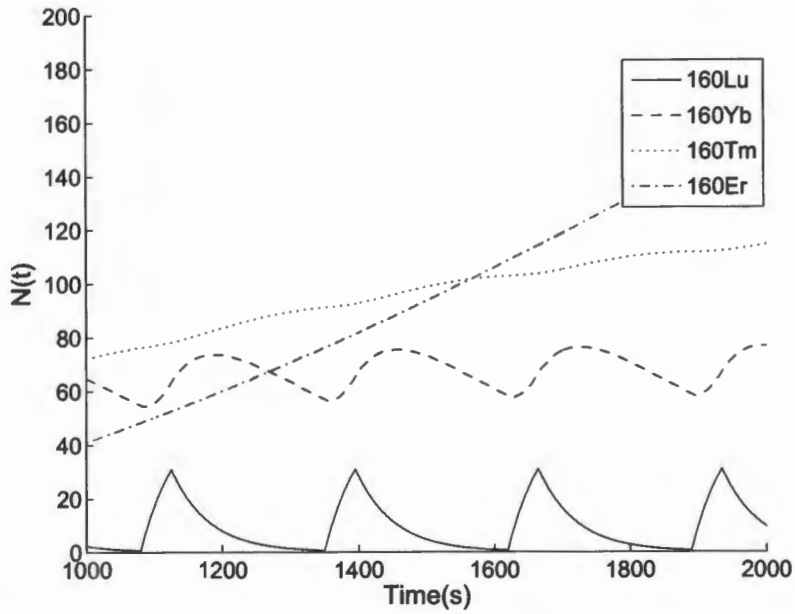

Figure 3.8: A plot taken from figure 3.7 between the time 1000 and 2000 s to actually see the ^{160}Tm line.

with a rhombicuboctahedron shape which can hold up to 16 detectors. There are two types of detectors in the AFRODITE array, namely the clover (high energy γ-ray detector surrounded by Compton suppression shield) and LEPS (low energy photon spectrometer) detectors. Originally the AFRODITE frame was designed to hold up to 8 clovers and 8 LEPS but this arrangement can be modified to suite the measurement required. For example, in this experiment, since we were interested in high energy γ rays, we reduced the number of LEPS detectors to 3 and used 9 clover detectors. Figure 3.10 shows an open view of the AFRODITE array with clover detectors surrounded by suppression shields and LEPS detectors and the target chamber supported by the beam line. Each detector consists of a 2.5 litre liquid nitrogen dewar. For low-noise perfomance, the input stages of the preamplifier are cooled to reduce electronic noise. The dewars are filled with liquid nitrogen (LN_2) from an automatic liquid nitrogen cooling system which was designed and built in order to keep them cool and to monitor the individual detectors. This picture was taken after the experiment and the setup may have be different. The advantage of using as many detectors as possible is that large numbers of events can be detected.

3.5.1 Clover detector geometry and the modes of detection

To detect high energy γ rays 9 clover detectors were used. They consists of four co-axial n-type Germanium crystals arranged in the configuration of a four leaf clover packed together as shown in figure 3.9. The crystals are held together by the rear side, thus reducing the quantity of material surrounding the crystal and improving the peak-to-background ratio. The individual crystals for clover are 50 mm diagonally and 70 mm long. The tapered germanium crystals are packed very close together to improve the addback factor and the distance from one germanium crystal to the other is typically 0.2 mm [Duc99].

When energetic incident γ rays interact with the detector's volume it may be in three possible ways. The photon's energy deposited into the detector volume can be fully absorbed in the crystal in a process known as the Photoelectric effect or the photon can also undergo scattering in the detector crystal and lose some of its energy which is known as Compton scatterings. The third process is pair production, when a high energy γ ray interact with the detector forming an elementary particles electron and positron pair from the electromagnetic radiation traveling through the matter.

In the event where the γ rays have Compton scattered photons escaping from one crystal are detected in a neighboring crystal. Adding the signals corresponding to vertical and horizontal scattered events between adjacent crystals, enhances significantly the efficiency of the clover detectors and is called the "addback" mode. In this mode, coincident events in different crystals are summed, resulting in the reconstruction of full-energy signals if Compton-scattered or 511 keV annihilation photons escaping from one crystal are detected in a neighboring crystal. The summed signals are stored in the addback spectrum, which results in an improved full-energy peak efficiency at the expense of the Compton continuum and escape peaks. The addback mode is an excellent tool for detecting high energy γ rays ($\geq$ 2MeV). Thus the advantages of the clover detectors are that it has high-energy resolution and high-detection efficiency of high energy γ rays.

3.5.2 BGO Compton suppression shield

A typical naked germanium detector gives a spectrum for monoenergetic 1 MeV γ rays in which a photopeak has only 20% of the counts and 80% are in a continuous background of lower energy. This background is caused mainly by γ rays which do not deposit their full energy in the germanium detector volume and lead to a large Compton continuum, known as Compton scattering. In order to suppress the contribution of scattered γ rays,

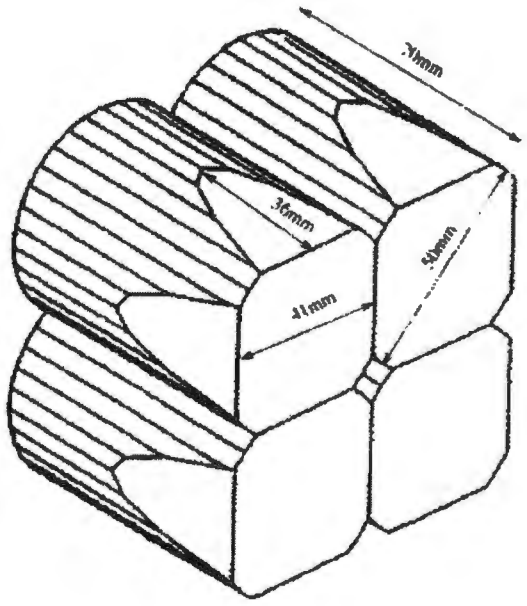

Figure 3.9: A schematic diagram showing how the four co-axial n-type Germanium crystals are packed in a Clover detector [Jon95].

the germanium detector was surrounded with BGO (Bismuth Germanate of the composition $Bi_4Ge_3O_{12}$) scintillation detector system, used to detect the escaping scattered photons. When the escape photon is detected, the events may be suppressed from the spectrum electronically. BGO scintillators are pure inorganic scintillators. Suppression of the Compton continuum is the most effective method to reduce the background in the region of full-energy peaks in multichannel analyzer spectra. The clover and BGO detectors are operated in anti-coincidence, which means that if a γ ray interacts with both detectors at the same time then the event is rejected. The BGO was used because of its excellent timing properties and high density ($7.13 g/cm^3$), so a relatively small amount of material is needed in order to reduce the energy of the scattered photons. Since BGO has the large atomic number of Bi ($Z = 83$), it has a high efficiency in detecting γ rays. In front of the shield there is a heavy collimator which prevents the γ rays from interacting with the BGO material, as the event will be rejected.

3.5.3 Low energy photon spectrometers (LEPS) detector

Unlike the clover detectors, the LEPS detectors are not placed inside BGO suppression shields, because photons of low energy are less likely to Compton scatter out of the crystal. LEPS detectors are made of a single crystal of p-type HPGe electrically segmented into four quadrants. It consists of a cooled planar detector and a preamplifier [Kno00]. The consequences of the planar geometry is that LEPS efficiency falls off much fast with increasing energy than that occurs in clover detectors.

3.5.4 Target chamber and the target ladder

The AFRODITE target chamber is made of aluminum material. It has the same geometry as that of the frame and has thin aluminium windows on the 16 square faces facing the clover and LEPS detectors. The chamber was design to afford a direct view of the target frame mounted onto a ladder through a facet. The two facets at angles 0° and 180° were connected to the beam line. The window at an angle 90° supported the target ladder at a position perpendicular to the beam direction. These windows are transparent to the γ rays and also maintain a good vacuum. There is a round window made from transparent glass on the target chamber that supports the camera, which helps to focus the beam through the ruby hole. This camera is connected to the computer in the control room where they adjust the beam to reduce the halo around the ruby hole during the experiment. Individual solid targets are mounted on a vertical ladder assembly that is retracted into a window at an angle 90°, which protrudes through a target chamber hole. Figure 3.11 shows the target chamber with its aluminium windows.

3.6 AFRODITE electronics and data acquisition

When the clover and LEPS detectors fire, the processing of signals from the preamplifier is done by the Nuclear Instrument Module (NIM) and CAMAC modules located in the experimental vault. Logic diagram for processing the signals from clovers and LEPS for the AFRODITE array is shown in figure 3.12. The LEPS detectors provide four channels per detector. The N568 amplifier amplifies the signals from the LEPS preamplifier and shapes them in a convenient form for timing, while the 572 amplifier provides an energy signals to the 4418/V ADC. The fast signal produced by the N568 goes to the constant fraction discriminator (934 CFD) where the signal is converted to a logic form. The circuit

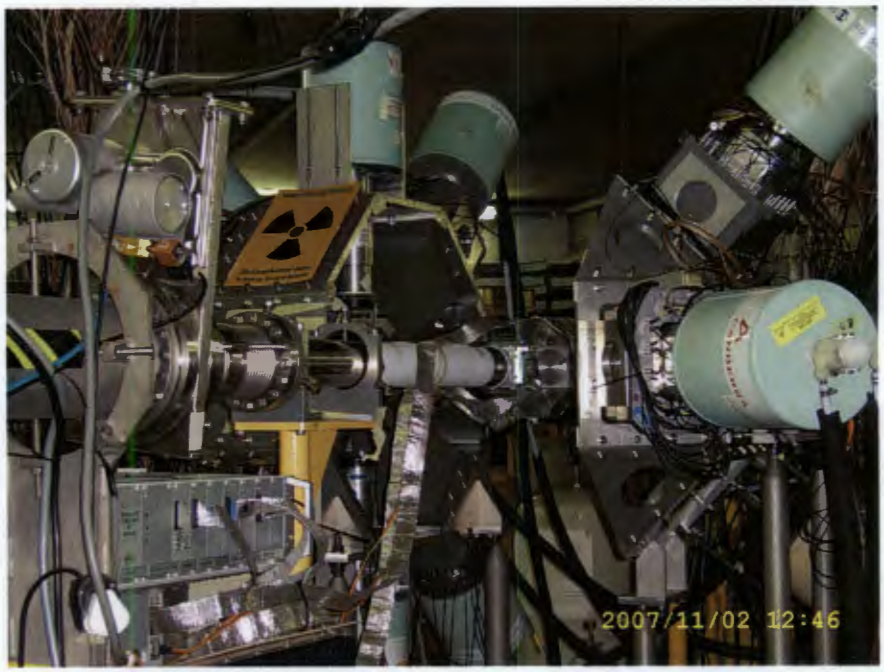

Figure 3.10: AFRODITE array with its frame which supports the clovers (surrounded by the BGO shield) and LEPS detectors.

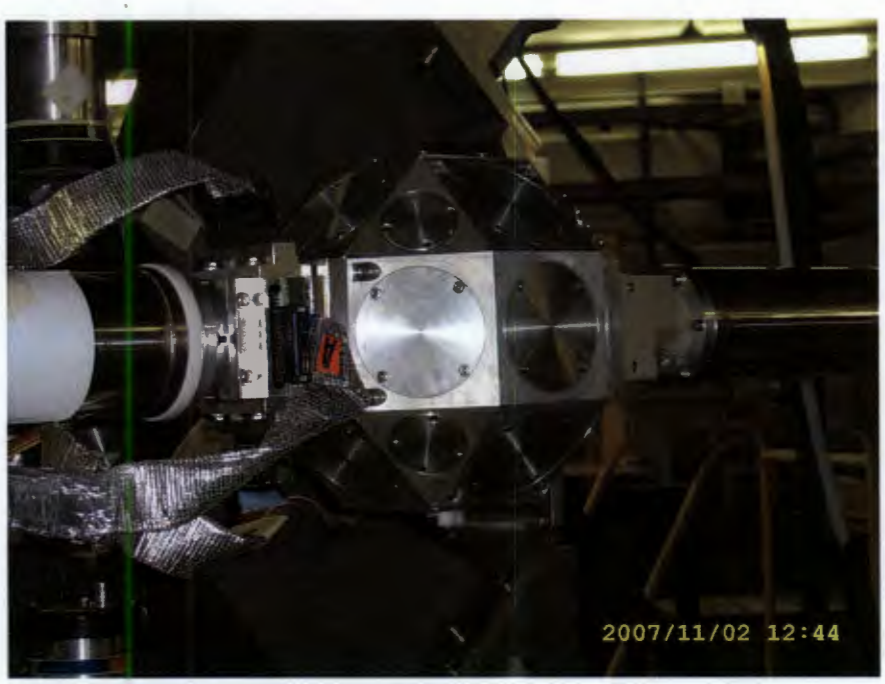

Figure 3.11: The rhombicuboctahedron-shaped target chamber has a total of 16 aluminium windows. The target chamber is supported by the beam line.

accepts input signals from all four channels to form an OR output. The LEPS signals are fed into the multiplicity units which give selectable logic output depending on the number or multiplicity of inputs which have fired. The fast signals also go to the Gate and Delay Generator (G&DG), which delays the signals until after the LEPS times are measured. The signal processing from the clover detectors are handled by the RIS modules. These modules have integrated circuits, which perform many of the functions described for the LEPS, in one unit. It includes the standard fast-slow processing and the anti-Compton veto of events with a BGO signal as shown schematically in figure 3.13 and 3.14, to produce the clean Ge signal, which is then fed to the two trigger-logic multiplicity units. The first unit for this experiment was set to 1, i.e the trigger demanded one suppressed clover fired.

The output from both multiplicity units is then ANDed in the 365AL coincidence unit. In this way, more complex trigger conditions can be demanded. This unit has a VETO input. The signal from the ion-source indicating beam-on was applied to this input to VETO acquisition during the beam-on period. Once the trigger was generated, it was fanned out to the various ADC's, TDC's, and RIS modules. When one branch gated the Silena 4418/v ADC's, which digitised the LEPS's energies, another branch would enable digitisation of energy and time in the RIS module by gating the clean Ge signal of the RIS module back into itself, into its trigger input which would signal to the module to commence conversion. The RIS modules, 4418TDC's and 4418ADC's are readout on a FERA BUS by a VME module called F2VB and thereafter the data is sent out to a Linux workstation, which writes the data to DLT tape. This data is stored in an event mode and for each clover and LEPS. The detected event is a set of channel numbers representing the energies of the γ rays detected. The channel numbers are discretized representations of an analog signal obtained from an individual detector. The range of channel available is established by the electronics. For example, we have 0 to 4095 channels using iThemba LABS AFRODITE electronics. The slow time was recorded using a pulser, running at 10 Hz and a scaler to count the pulser. The scaler was zeroed and cleared at the beginnig of the beam ON cycle, and counting commenced. Once the 365AL was uninhibited at the beginning of the beam OFF period, data acquisition commenced. With the detection of a γ ray the scaler was read in this way giving the time of detection relative to the beginning of the beam ON period.

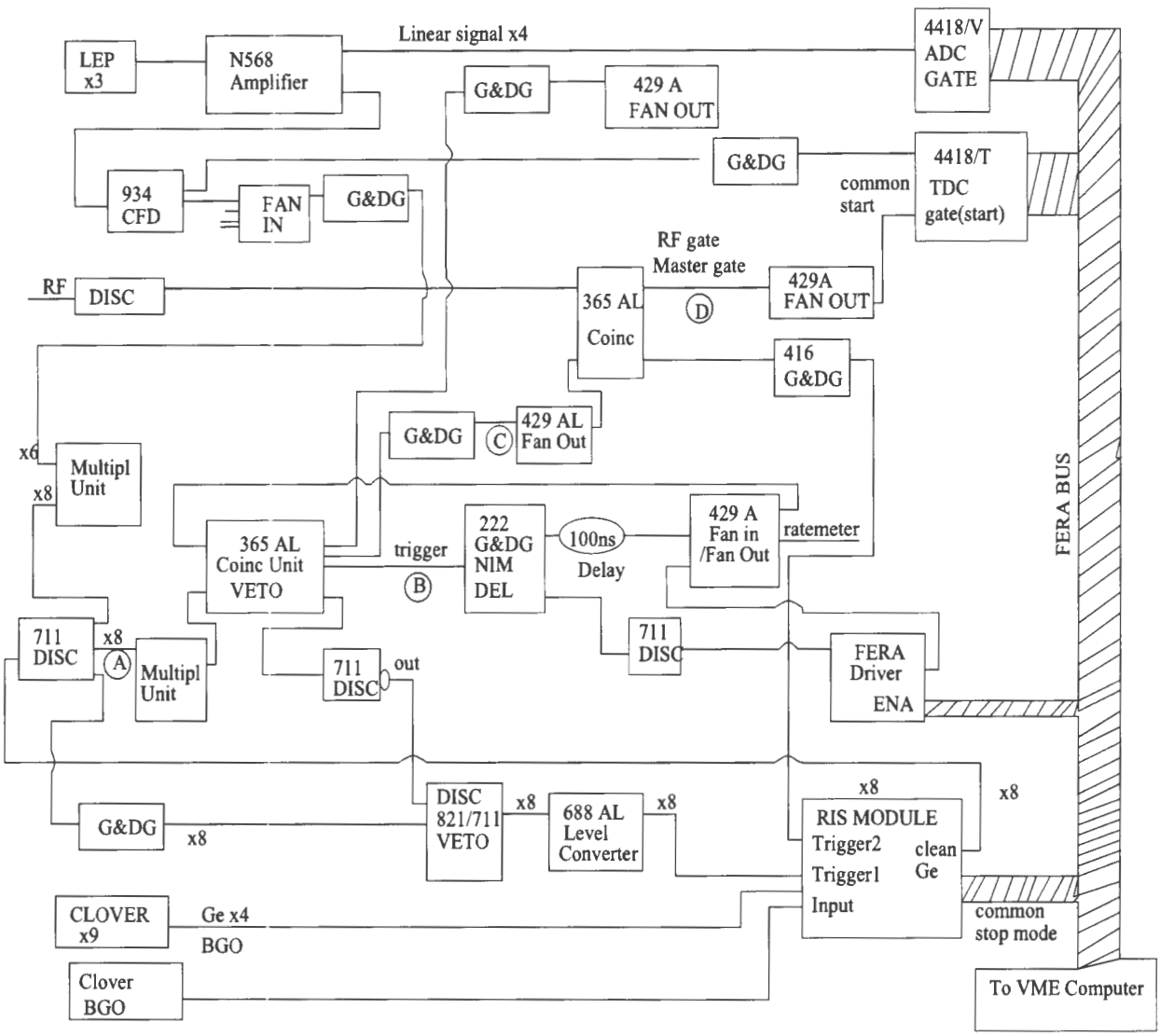

Figure 3.12: AFRODITE electronics logic diagram.

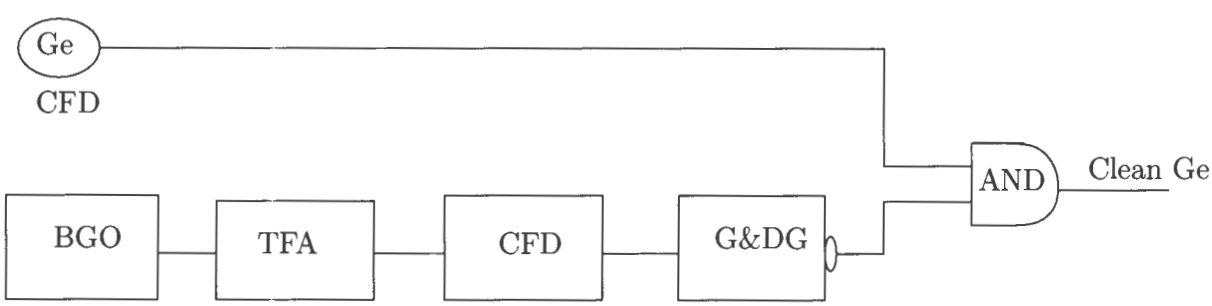

Figure 3.13: Logic diagram of RIS modules.

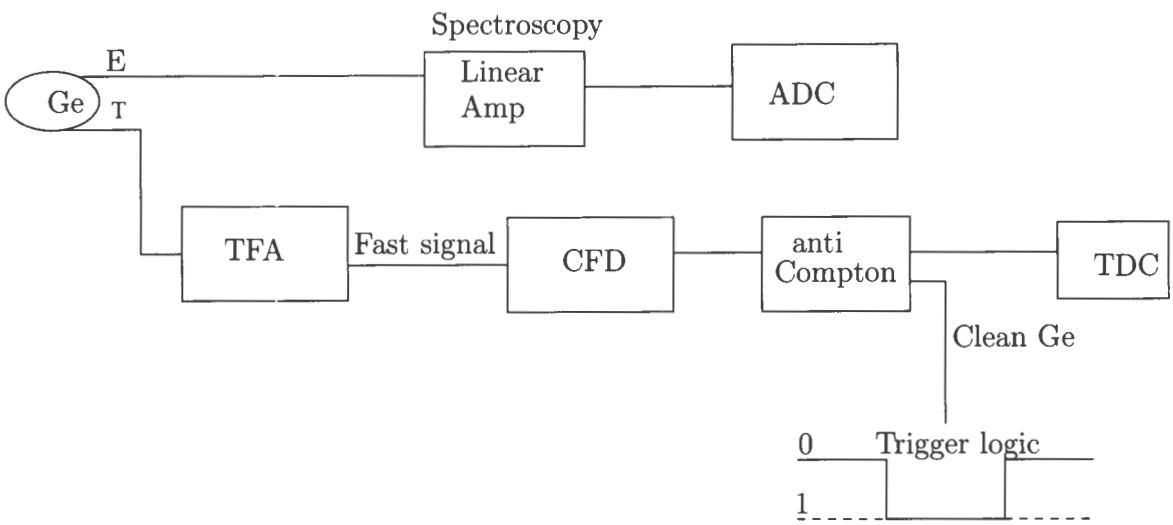

Figure 3.14: Schematic view of the Anti-compton part of the electronics process occuring in the RIS modules with BGO.

Chapter 4

Data analysis procedure

Before the data was stored to tape, some inspection of the data was performed during the running of the experiment to confirm if the reaction was giving the expected results by viewing the online γ-ray spectra. Once the strong peaks from the nucleus of interest were identified, the data started to be stored to tape. By the end of the experiment, a large amount of data was stored on tape for archival purposes. After the experiment, the data stored on the tape was copied to a disk of a large memory computer ready to be sorted. The computer program Midas MTsort was developed [SamMTsort] to sort the data offline into matrix form. A matrix is a two dimensional histogram, in this case with a channel range of (0, 4095) on each axis. This allows a fast examination of correlations between γ rays, exposing pairs more likely to occur in the same event and, hence, in the same cascade. During the experiment the event trigger was set to single γ rays, but both $\gamma - \gamma$ coincidence and single γ-ray data were acquired in event mode.

The RadWare [Rad95] software packages were employed to examine the matrix after sorting and were mostly used in the data analysis. The RadWare programs used were GF3, EFFIT, and the ESCL8R.

4.1 Energy calibration and gain matching

In order to properly identify the various γ-ray peaks in the spectrum from the detectors, the detector must be calibrated. A radioactive γ-ray source is conventionally used to supply peaks of known energy in the spectrum. Here we used two radioactive γ-ray sources, ^{133}Ba and ^{152}Eu, with γ-ray energies that are not widely different from those to be measured in the

unknown spectrum. The ^{152}Eu source has a γ-ray spectrum with energies ranging from 40 to 1407.5 keV, while the ^{133}Ba has a γ-ray spectrum with energies ranging from 53 to 383 keV. The relative intensities for these radioactive sources are well-known [Led67, Fir96]. These two sources were used to avoid the non-linearity of the spectrometer. The energy calibration was done before the start of the experiment. The sources were placed on the target ladder inside the target chamber and the data was recorded in event mode. The relations between the ADC channel x and the γ-ray energy for the clover detectors is parametrized using the quadratic equation,

$$E_\gamma = a_2x^2 + a_1x + a_0, \tag{4.1}$$

where a_2 and a_1 are the coefficients and a_0 is the constant. Prior to the data sorting, the data from each detector should have a constant energy dispersion. This process is termed as gain matching, gain matched channel $x' = \frac{1}{epc}E_\gamma$, where E_γ is the energy corresponding to an ADC channel x and *epc* (energy per channel) was chosen to be 1 keV/channel for 4096 $\times$ 4096 γ-γ matrices. The gain matching for all germanium detectors was performed after the energy calibration.

For the clover detectors, with a quadratic energy calibration, $E_\gamma = a_2x^2 + a_1x + a_0$, the old channel x was mapped onto the new channel x', with a linear calibration of $E'_\gamma = x'$. This was done by equating the two equations of energy as follows:

$$E_\gamma = x' = a_2x^2 + a_1x + a_0. \tag{4.2}$$

The program DOP_COR was used to calculate the gain matching coefficients, and they were used to map the channel to the energy calibration $E = x$ for the clover detectors. The use of the quadratic term was important because detector's response was found in several case to be non-linear. This non-linearity originates from the electronics used and is not identical for all the detectors.

4.2 Efficiency calibration of a germanium detector

The detection efficiency for γ rays (required for the clover detectors) changes as a function of γ-ray energy. In this work, the efficiency calibrations were performed using the known γ-ray intensities from the ^{133}Ba and ^{152}Eu radioactive sources. The efficiency calibration measurements for the clover detectors were performed at the end of the experiment. The γ-ray sources were placed in the target ladder inside the target chamber and the γ rays were allowed to strike the detectors after passing through same materials present during the

experiment. This was done to obtain the correct attenuation of the γ rays to the detector.

The efficiency calibration data was sorted offline using the MTsort program and the output spectra were converted into RadWare readable format using the eg2rad command. Using the RadWare GF3 program, the peak areas and centroids were found. The RadWare EFFIT program was used to fit the data points obtained from the two γ sources from the 9 clovers. Figure shown in 4.1 is indicating how the relative efficiency ε of the detector changes as a function of energy. The total efficiency calibration of the germanium detector is given by:

$$\ln(\epsilon)_{\text{total}} = \ln(\epsilon)_{\text{l}} + \ln(\epsilon)_{\text{h}}, \tag{4.3}$$

with the efficiency at low energies

$$\ln(\epsilon)_{\text{l}} = A + Bx + Cx^2, \tag{4.4}$$

and the efficiency at high energies

$$\ln(\epsilon)_{\text{h}} = D + Ey + Fy^2. \tag{4.5}$$

The coefficients A, B, C, D, E, F are the fitted parameters. The ^{133}Ba source was used to determine the turning point of the curve near 150 keV. The efficiency of the detectors decreases steeply as the photoelectric effect decreases, and at higher energies there is a large probability that the γ rays will not interact with the crystals. For the γ rays which scattered and lost energy in different crystal we used the addback efficiency parameters to get the total energy of the peak.

4.3 Construction of γ-γ and γ-Time matrices.

The time we had to collect data from one weekend of beam time was 38 h, and the data was sorted offline using the Midas MTsort program into two types of matrix. The energy and efficiency calibration parameters that were obtained were used in the MTsort program. The matched energies were used to update a two dimensional (E_γ,E_γ) matrix from the $\gamma - \gamma$ coincidence data, **MATRIX(γ_1,γ_2)= MATRIX(γ_1,γ_2)+1**. For the γ-Time matrix, the matched energy and time were used to update a two dimensional (γ,time) matrix from single γ ray's data, **MATRIX(γ,time)=MATRIX(γ, time)+1**. In order to identify from which nuclei single γ were emitted, the γ-Time matrix was used to give easy access to the decay curve for half-lives determination. Because we were mostly interested in high energy

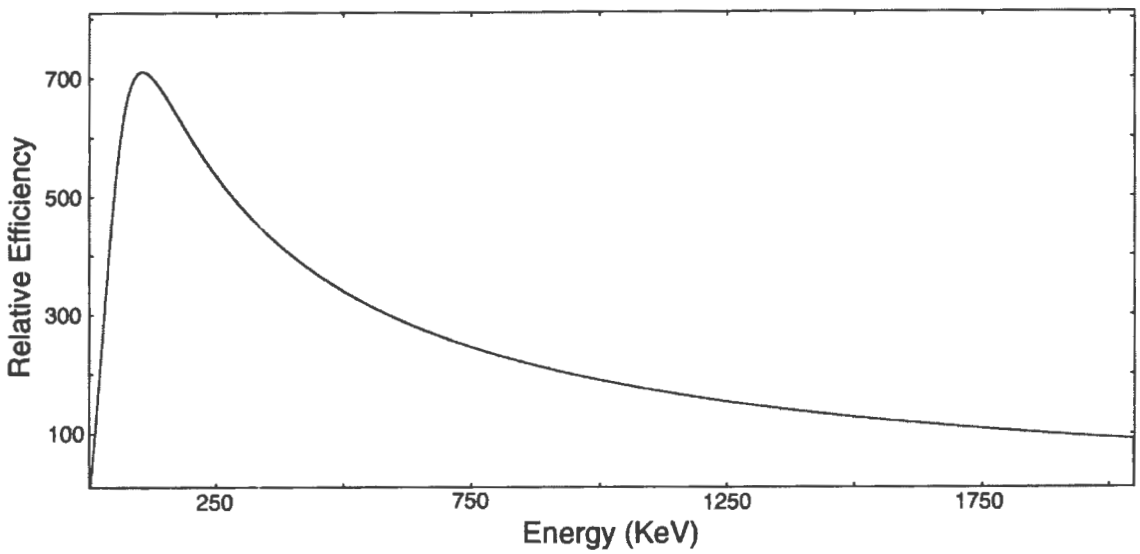

Figure 4.1: Efficiency curve of the HpGe clover γ-ray detector using the ^{152}Eu and ^{133}Ba sources.

γ rays, we decided to give first priority to the data from the clover detector. The analysis of data from LEPS is in progress. The clover detectors are very efficient in measuring high energy γ rays as compared to the LEPS detector. The two matrices were in MIDAS readable format and then the eg2rad command was used to convert the two dimensional spectra into a (.mat) RadWare readable format, which can then be analysed with the GF3, ESCL8R and other programs. Both matrices with (4096×4096) channels have 1 keV/channel dispersion.

4.3.1 The $\gamma - \gamma$ coincidences

The γ-γ matrix was only updated if two of the γ rays occurred within an interval of 150 ns of each other. This relatively long interval was used to include low energy γ rays (including X-rays), which can suffer from time walk in the HpGe detectors. Figure 4.2 is the total energy projection spectrum from the 2-D symmetric γ-γ matrix. A Background-subtracted spectrum was then generated with the program GF3 from this spectrum, and the γ rays were examined to construct the level scheme using the ESCL8R program. This program requires the 2-D γ-γ matrix, parameters from the efficiency and energy calibrations, a total projection spectrum and a background subtracted spectrum to build the level scheme.

The yield of ^{160}Yb from β^+-decay was much less than anticipated because, in the reaction, ^{160}Yb was unexpectedly populated twice as strongly as ^{160}Lu. About 765 thousands of $\gamma - \gamma$

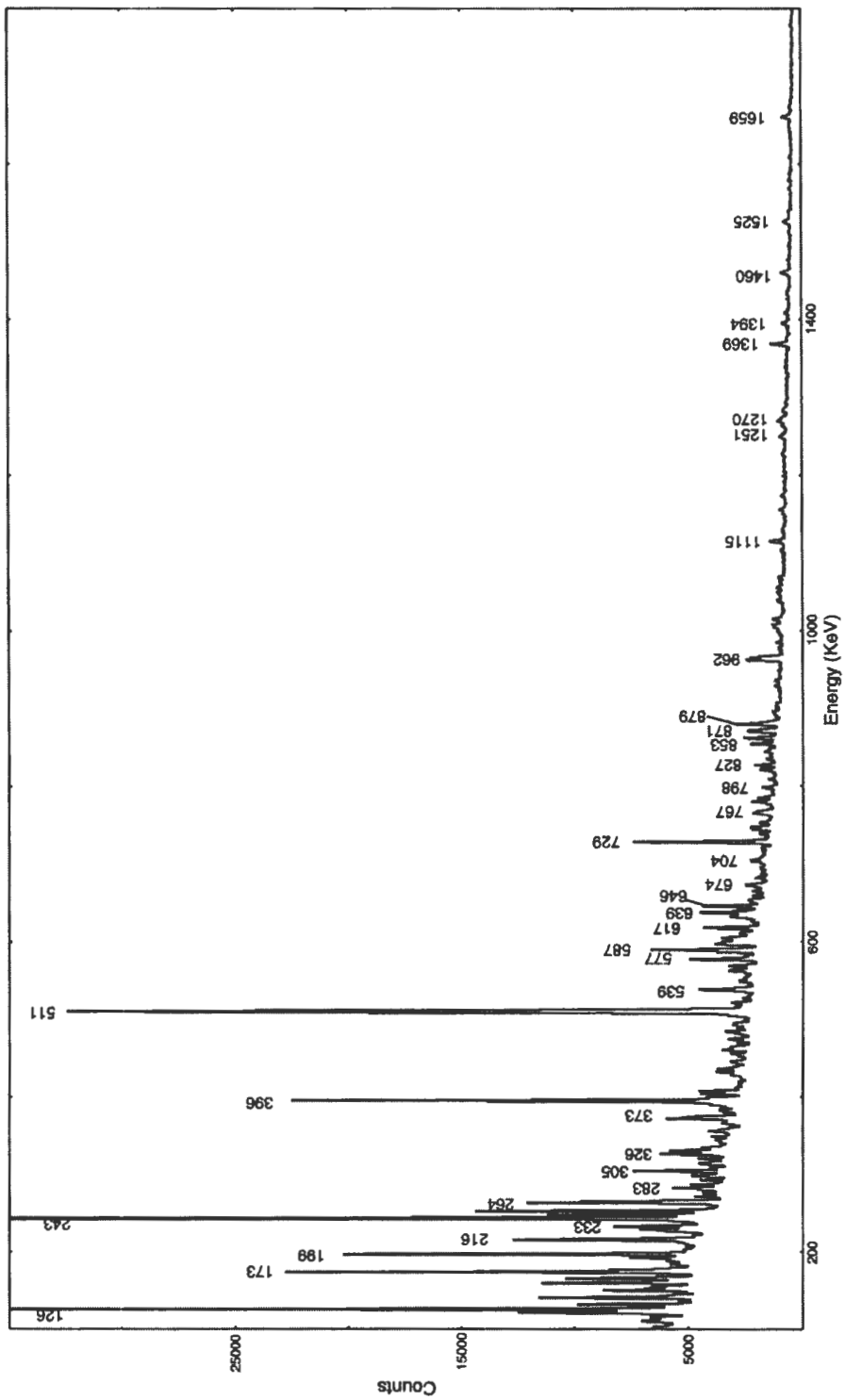

Figure 4.2: Total energy projection from the γ-γ matrix.

coincidences were acquired. This statistics was small and limited us in observing many new states we thought we could observe with the AFRODITE array.

γ-γ matrix peak identification

There are many peaks in the spectrum obtained from γ-γ matrix (shown in figure 4.2). Some strong peaks are known to come from ^{160}Yb, for example, at 243, 396, and 577 keV, but for the unknown peaks examination of the coincidence spectra was done to establish the decay path. We had to identify whether it is coincident with other γ rays by setting the gate at the γ-ray peak of interest. Once it is identified, a γ-ray transition is added into the level scheme.

In order to get the 243 keV coincidence spectrum shown in figure 4.3, the gate was set on the γ-γ matrix by entering the desired energy or limiting channels to the program ESCL8R. In this case, we can only see the transitions which are above the gated transition. For example, all the strong peaks in the spectrum follow the same decay path of the gated transition. The transitions which are in other bands and do not follow the decay path of the gate transitions are not observed. A gate was set on the 1512 keV γ-ray peak resulted in the coincidence spectrum shown in figure 4.4, where 243 keV that is in coincidence with the gated transition appeared. The 1055 and 1582 keV γ ray were identified to come from ^{160}Yb by setting a gate on each of them and found that they are both in coincident with 243 keV γ ray but the decay path is different.

There are peaks which are in mutual coincidence but are not placed in ^{160}Yb. For example, the 437 keV line is found to be in coincidence with the 1226 keV and 1525 keV line as shown in figure 4.5. In the spectrum the 243 keV and 396 keV peaks from ^{160}Yb has appeared, because of the 435 keV which is in ^{160}Yb. The 1227 keV gated spectrum, shown in figure 4.6, shows strong peaks at 437 and 1525 keV which are in coincidence with the gated transition. This is good evidence to conclude that 1525 keV, 437 and 1227 keV γ-ray peaks are in mutual coincedence. The assignment of these peaks will come after the half-lives have been measured and is explained in the next section.

4.3.2 The γ-Time matrix analysis

The energy projection of the γ-Time matrix is shown in figure 4.7. The spectrum has many peaks and is rather complicated. It is not clear which peaks belong to ^{160}Yb. The activities of β^+-decay daughters are present in the spectrum. The calculations of the β^+-decay daughter

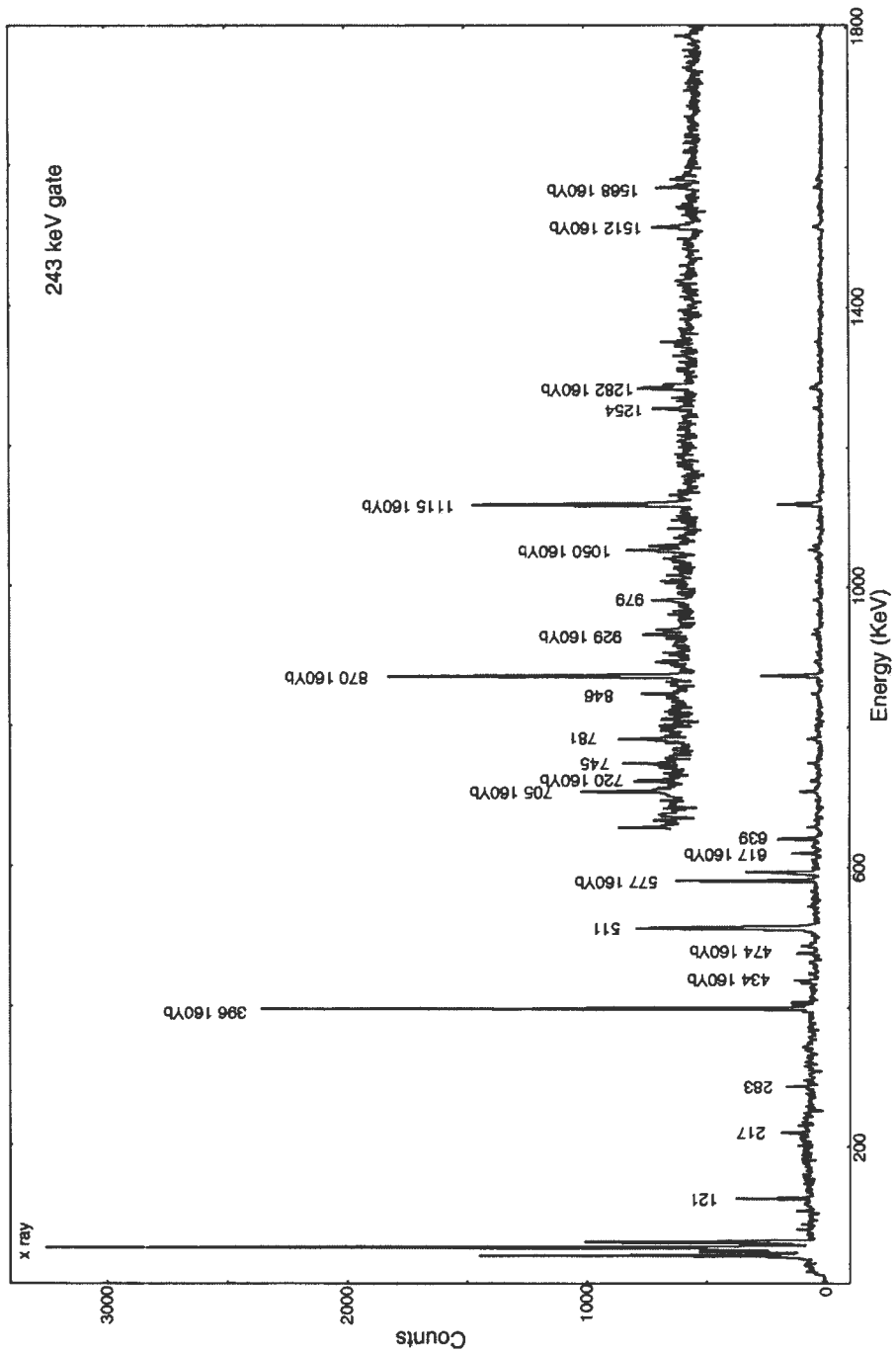

Figure 4.3: The energy spectrum of 243 keV gate from the γ-γ matrix.

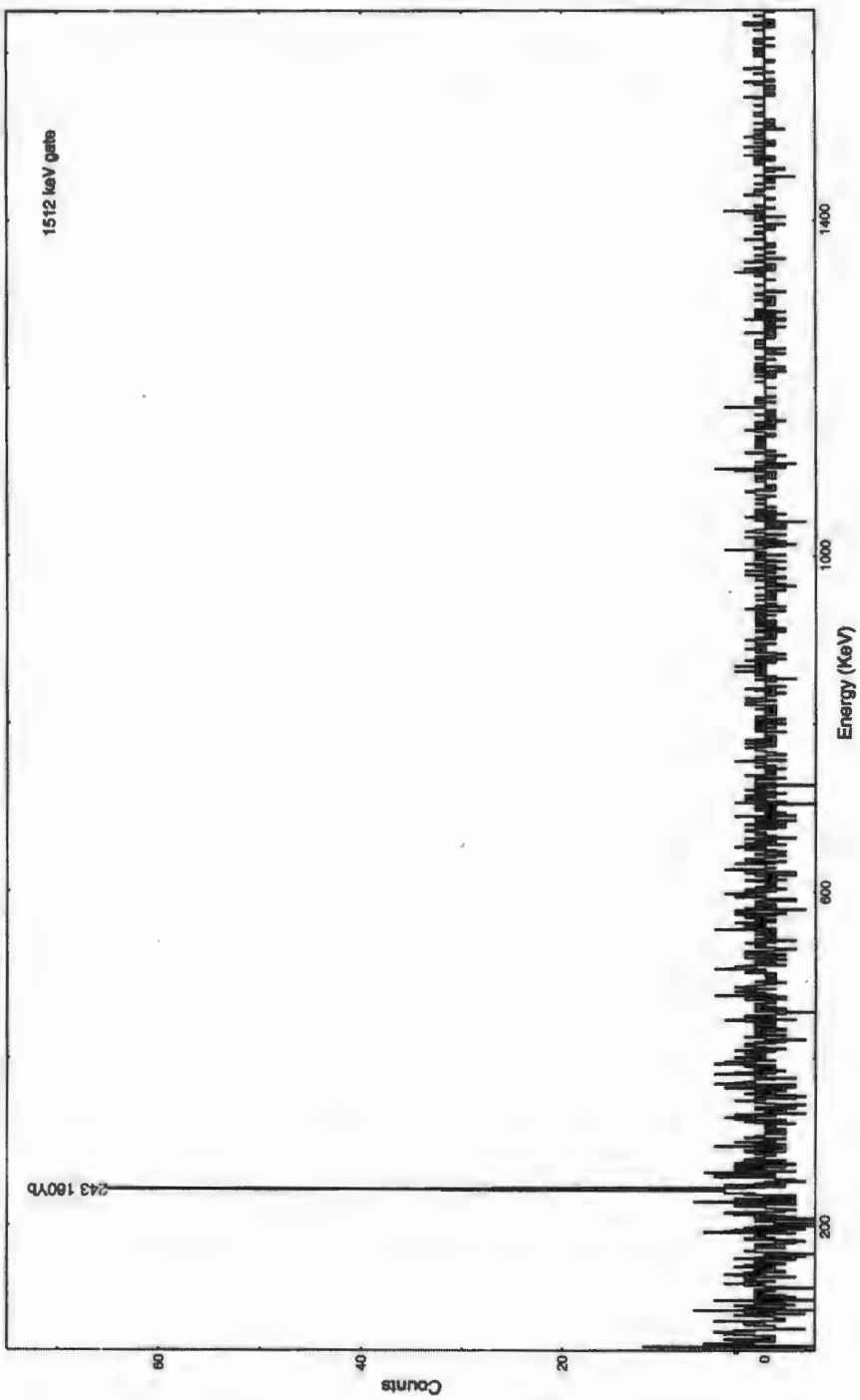

Figure 4.4: The energy spectrum of 1512 keV gate from the γ-γ matrix.

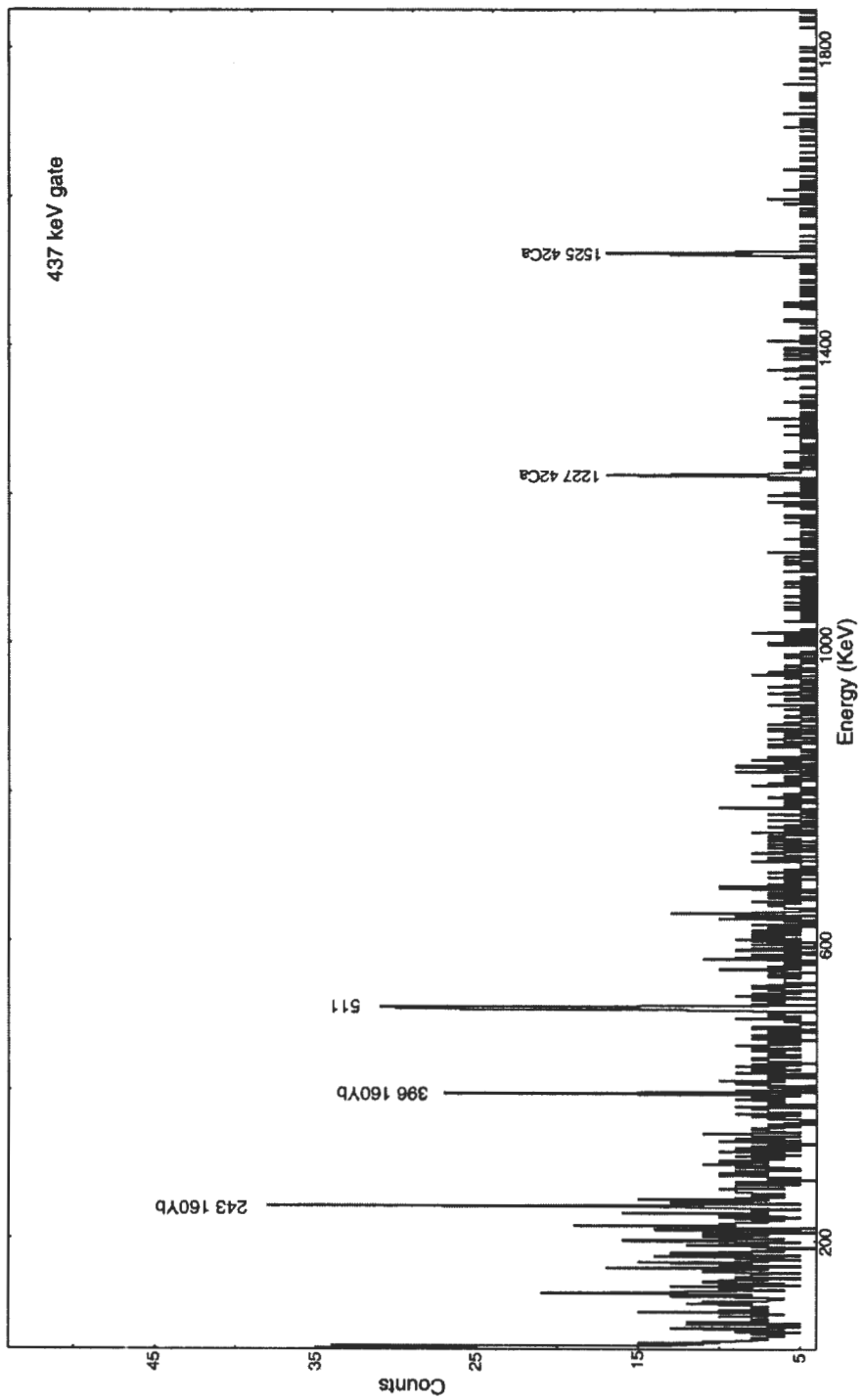

Figure 4.5: The energy spectrum of 437 keV gate from the γ-γ matrix.

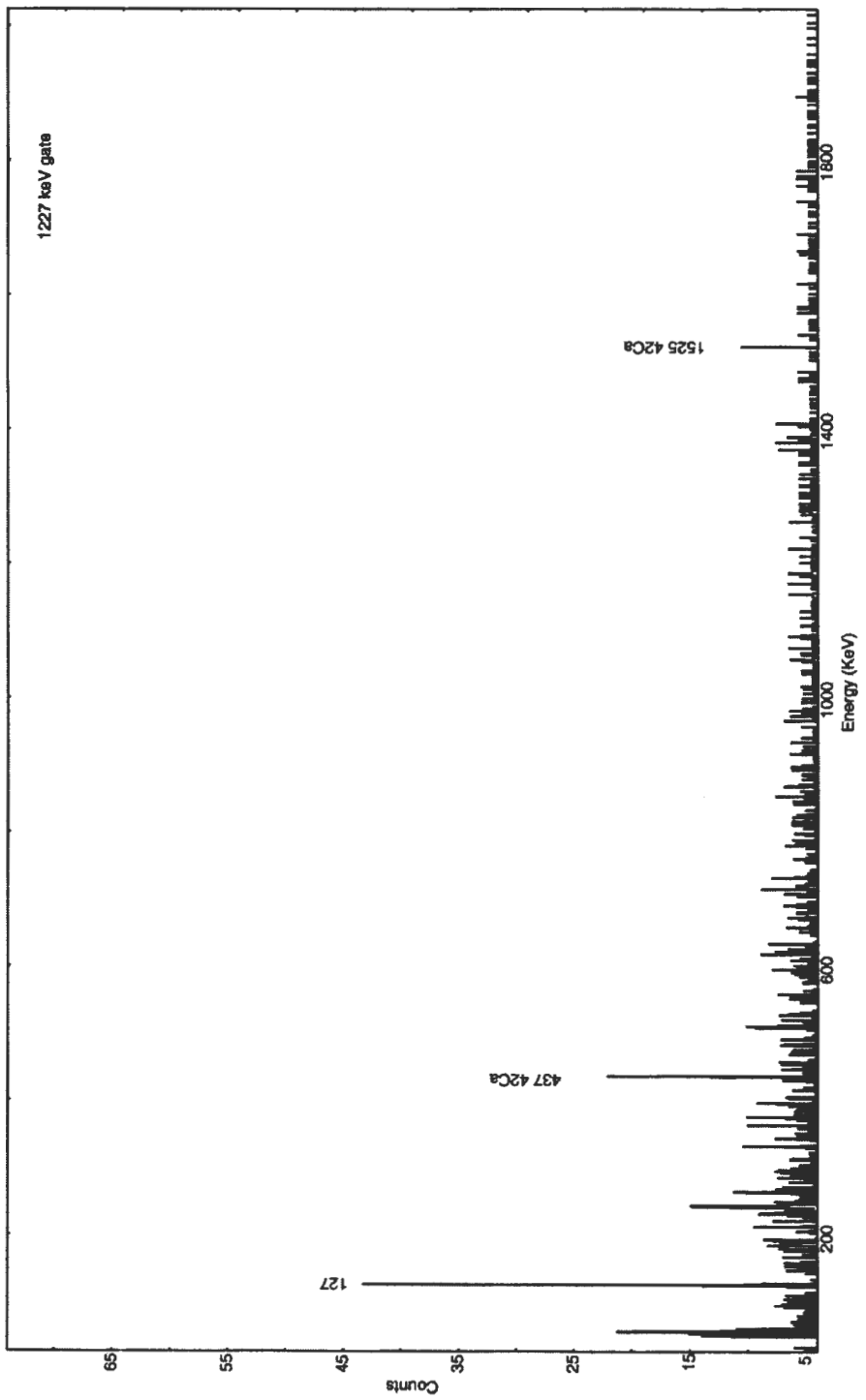

Figure 4.6: The energy spectrum of 1227 keV gate from γ-γ matrix.

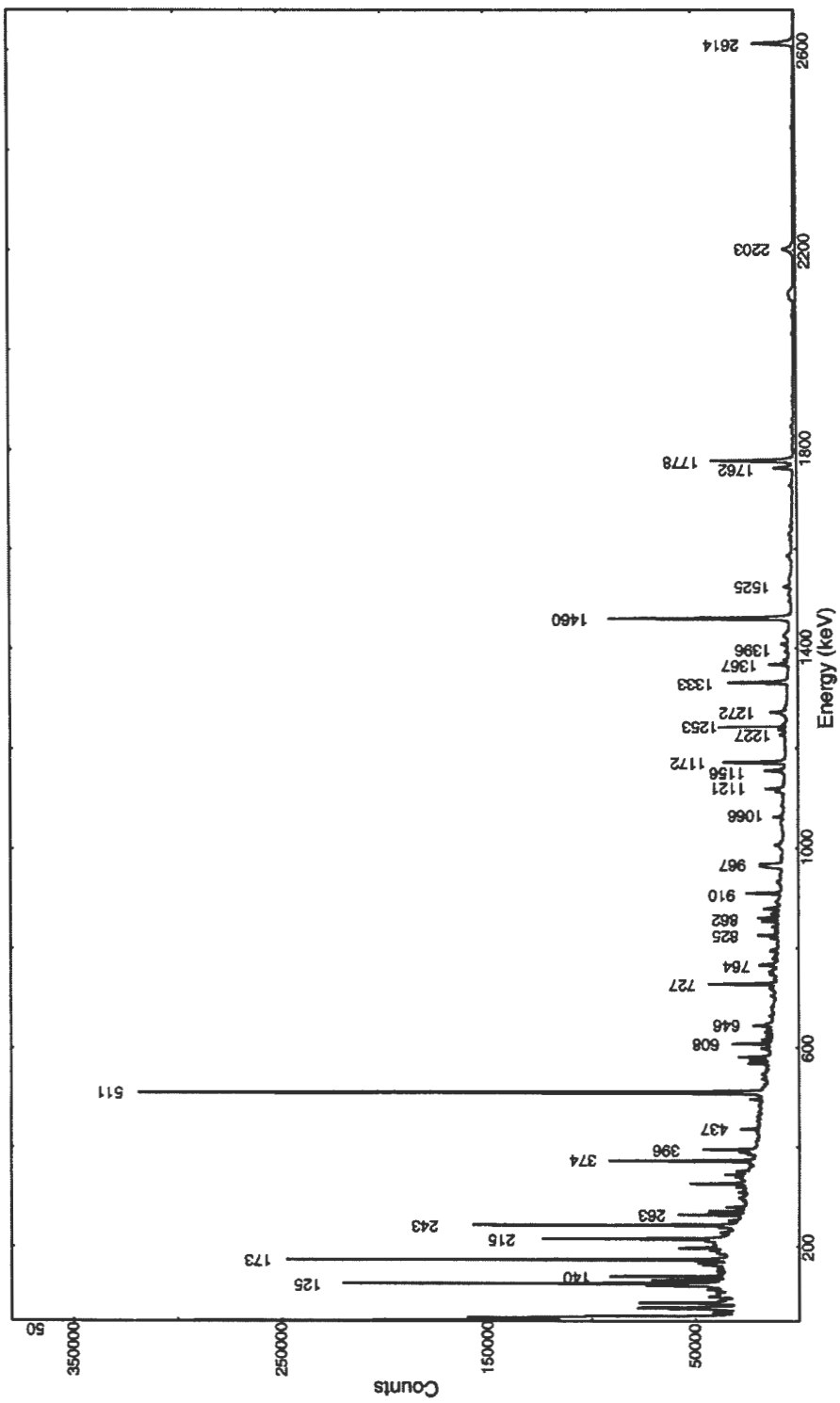

Figure 4.7: Total energy projection from the γ-Time matrix

populations suggest how to reduce the number of γ rays which come from the long-lived daughters. In figure 3.7, we can see that the population of ^{160}Tm is constant or has reached equilibrium by the time around 2500 s to the end of the beam time. We made use of this result to be able to reduce the number of γ rays belonging to ^{160}Er from the decay of ^{160}Tm. In the analysis, the time projection spectrum was divided into two equal parts, as seen in figure 4.8. There is an early part from time 48 to 159 s and a late part from 160 to 270 s. Since activities from the long-lived daughters are constant over this time interval, subtracting the γ-ray spectrum obtained in the late part from that of the early part removes the activity from the long lived daughters.

The resulting spectrum is shown in figure 4.9, which we called the early-late spectrum. It was necessary to find out which of the peaks left in the spectrum had the same half-life as the parent nucleus ^{160}Lu. Some of the peaks which were present in the total energy projection spectrum (figure 4.7) are not seen in the Early-late spectrum. (For example, the strong peak at 1408 keV which is from ^{152}Eu.) This has reduced the work of measuring the half-lives of all the peaks in the energy projection spectrum of the γ-Time matrix, as only those visible in figure 4.9 are of interest.

Peak and background gating

In the γ-Time matrix analysis, half-lives of the γ rays are measured in order to identify whether they are emitted from ^{160}Yb. The challenge is when we gate on the peak of interest, we find that the gates consist of peak plus background. Since the half-life of the background is different to the half-life of the peak, background subtraction must be done to avoid the problem of background affecting the half-life measurements of the photopeak. Background subtraction had to be done for every peak that is visible in the early-late spectrum.

In order to do the background subtraction, we select the peak which we intend to measure the half-life of the γ ray and select an area near to the peak as representative of the background under the peak. The spectrum shown in figure 4.10 is an illustration of how the gate on the peak and the background is selected. It is plotted as a representative of the strong peaks.

From the spectrum the background area under the peak is indicated by the rectangle with lines and the black shaded area is selected as the representative background. The portion selected as the background for the gated peak was selected because it shows no peaks. These gates were set on the spectrum using GF3 with a mouse to mark the beginning and end channels of the peak and background in the total energy projection of the γ-Time matrix shown in figure 4.7. The lower limit is the beginning channel and the upper limit is the end

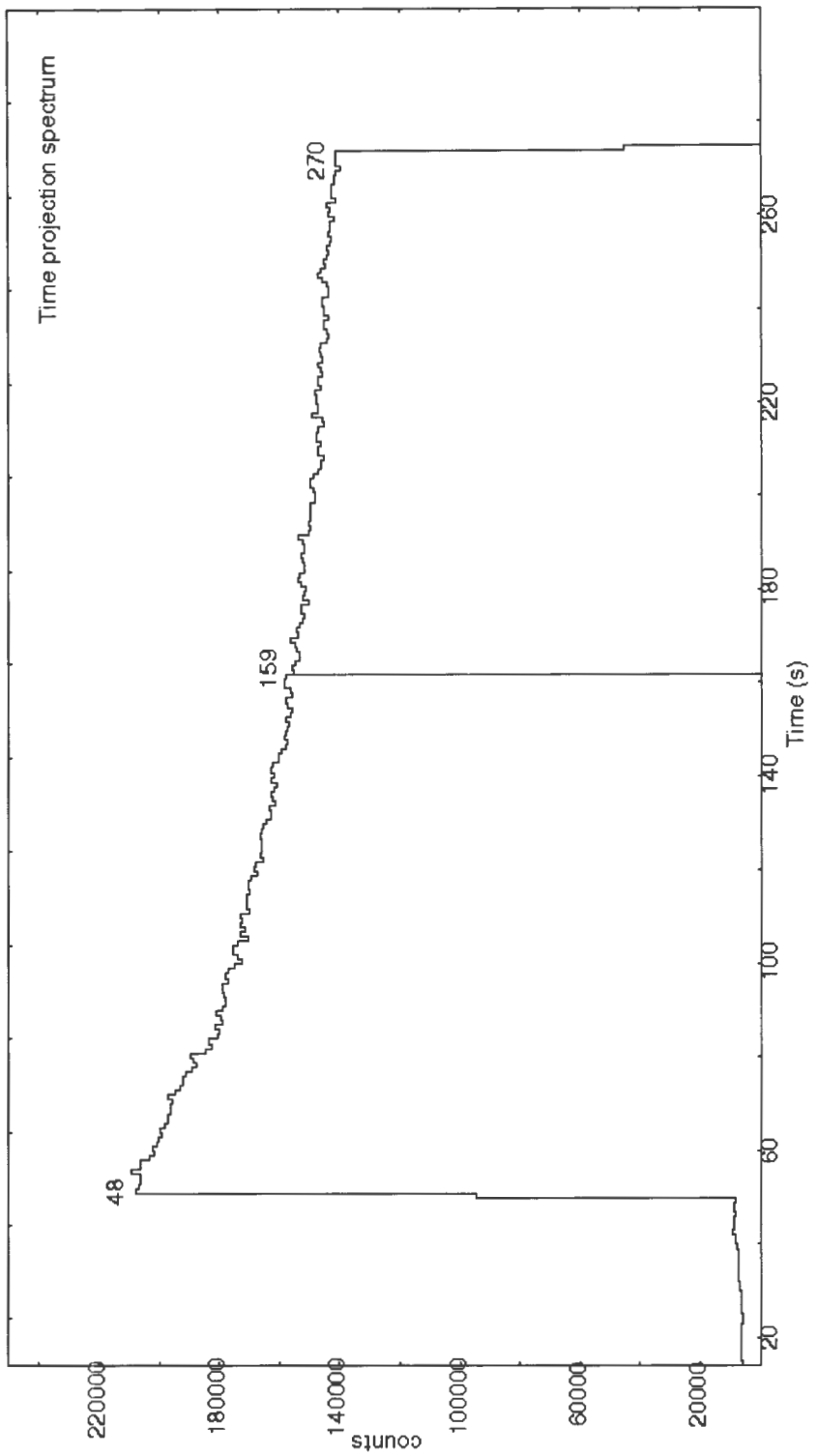

Figure 4.8: The time projection from γ-Time matrix

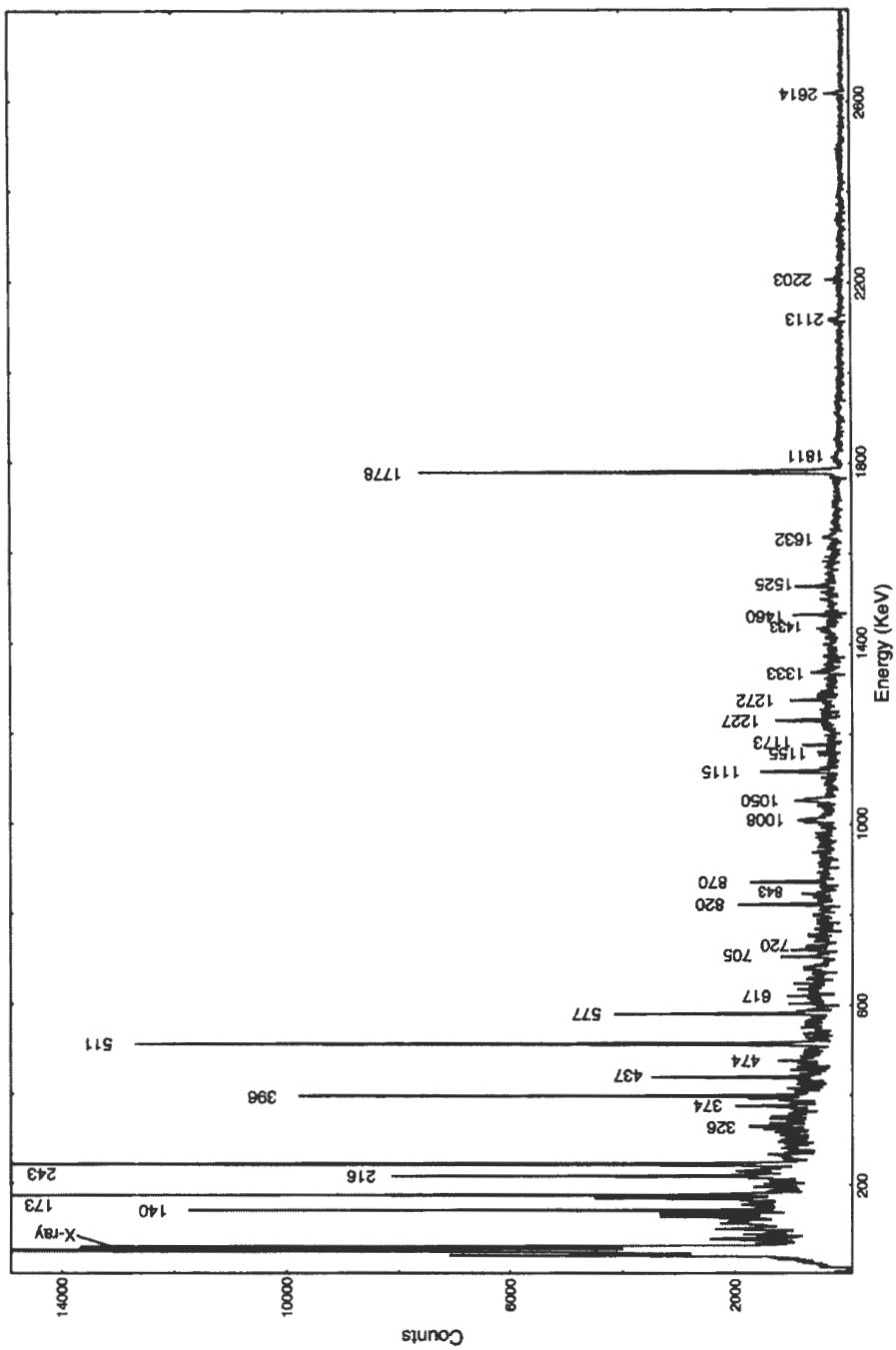

Figure 4.9: The resulting spectrum after the early part has been subtracted from the late part.

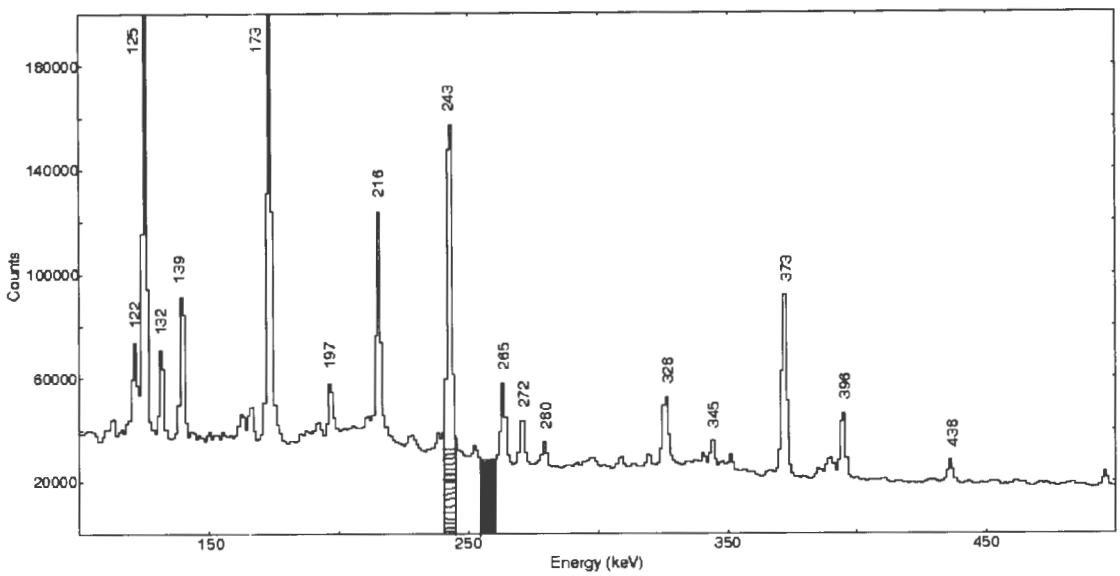

Figure 4.10: The spectrum indicating the gating of the peak and background for the strong at 243 keV.

channel of the peak and or background. The obtained channels are the inputs in the program GF3 that will slice the γ-Time matrix and display the requested channels as presented in figure 4.11, and is known as the gated spectrum. All the peaks of different energies and their backgrounds were marked in the total energy projection and gated in the γ-Time matrix in a similar way.

Background subtraction and nuclear half-life measurements

In this data analysis two techniques were used to measure the half-life of the γ-ray peaks. Initially the program GF3 was used to subtract the background from the gated γ-ray peak. The program GF3 performs the background subtraction by taking the peak gated spectrum and subtracting the gated background spectrum multiplied by the normalisation factor f. The resulting spectrum was then fitted with the computer program Root [BruRoo] to measure the meanlife τ. Normally the gated area under the peak should be equal to the gated area of the background, but if that is not the case, then f normalises the two. The normalisation factor f was determined by taking the area under the peak (rectangle with lines) and dividing it by the background area (shaded black rectangle). We calculated the area

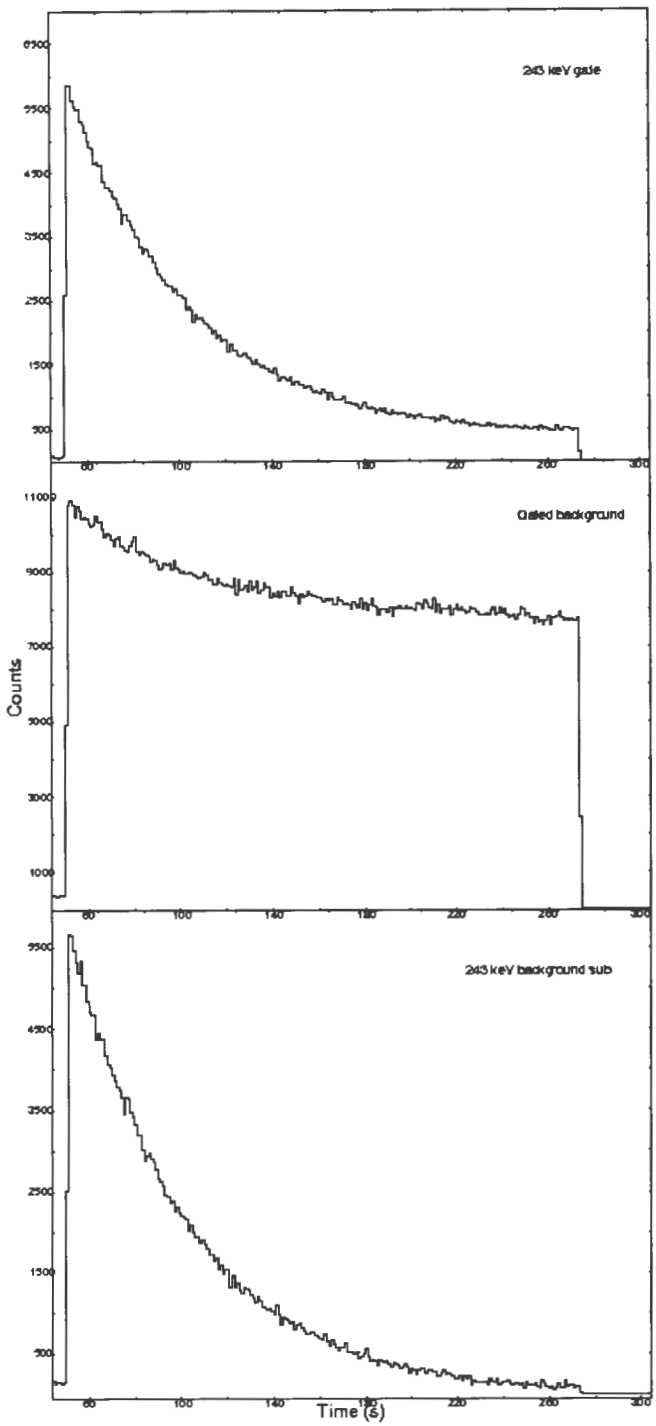

Figure 4.11: The time projection of 243 keV gated and gated background spectra from the γ-Time matrix. The top spectrum is the gate of the 243 keV γ-ray peak, the middle spectrum is the gated background which is selected for that peak. The bottom spectrum is the 243 keV gate background subtracted.

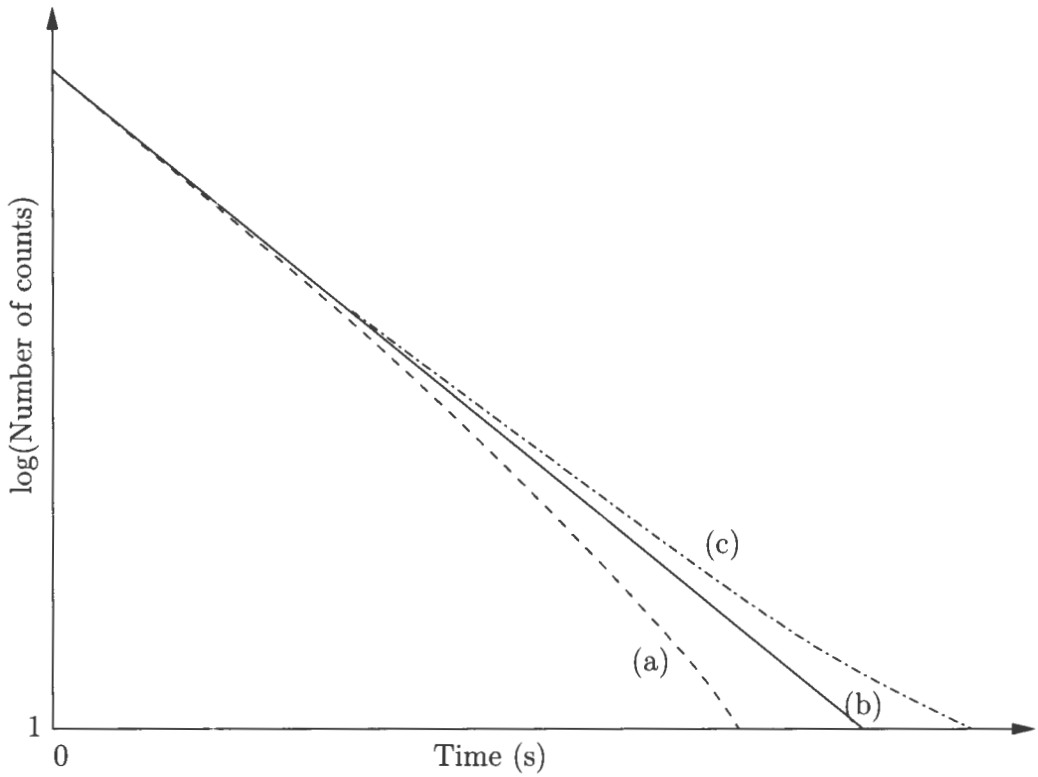

Figure 4.12: Schematic diagram illustrating the background subtraction.

under the peak by taking the difference of the channel from the beginning to the end of the peak plus 1 and multiplying this by the height of the background. The area of the background was also calculated in a similar way. This way of calculating the normalisation factor f was not accurate, because the background level for the peak was just an estimate. The resulting spectrum after background subtraction was also not accurate, implying the incorrect meanlife τ. In figure 4.12 (a) is a line indicating the peak counts which were over subtracted when background subtraction was performed. The line labeled (b) shows the accurate background subtraction, and line (c) illustrates that some background counts are left in the gated spectrum after background subtraction was performed.

This motivated us to use another program and compare the results. The program EONS was developed by Dr R. Bark to do the background subtraction and fit the spectrum to get the accurate meanlife τ. The advantage of using the program EONS was that it fitted the value of f, provided the initial value of f given was not too far from the correct one. The bottom Time projection spectrum in figure 4.11 obtained after the background has been subtracted from the top spectrum using the program GF3, using the value of f fitted with the program EONS. The slope is now given by an exponential decay law. To fit f, the program EONS

assumed that the spectrum gated on the peak is given by the function:

$$N(t) = N_0 \exp(-\lambda t) + fB(t), \tag{4.6}$$

where N_0 is the initial intensity of the γ ray, λ is the decay constant of the radioactive nuclei, B is the background spectrum and f is the normalisation factor, to normalise the gated peak spectrum with the background spectrum. The background spectrum was assumed to be described by the function:

$$B(t) = H_B \exp(-\lambda_B t) + C, \tag{4.7}$$

where H_B is the height of the background, λ_B is the decay constant of the background and C is the background constant. The program EONS would first take the spectrum gated on the background, and fit H_B, λ_B, and the background constant C. Next, the spectrum gated on the peak is read with EONS, and N_0, λ and f are simultaneously fitted with the parameters describing the background (H_B, λ_B and C) fixed.

The log plot of background subtracted spectrum of the 243 keV γ-ray peak is shown in figure 4.13. This spectrum is an example of one with good statistics and is identified as coming from the nucleus ^{160}Yb. The program EONS has improved the results. For example, the normalisation factor f calculated manually, for the 243 keV peak, was 0.109 but when the program has fitted the gated spectrum the factor was found to be 0.084. The fitted half-life was obtained to be 35.5(3) s.

Gamma-ray peaks of low energy generally have more counts than the peaks of high energy. This is because the efficiency of the detector to detect γ rays of low energy (see figure 4.1) is high and it decreases with an increase of the energy of the γ ray. The peaks which have few counts gave the program EONS a challenge. This is because when the peak is small compared to the background, small uncertainties in the background can have large uncertainties in the fitted half-life. One must be sure that region chosen to represent the background is actually representative of the background. For example, the background region labeled (d) in figure 4.14 could be considered to be comprised of numerous small peaks lying above the average background represented by the solid line. These peaks are substantial in area compared to the peak at 1227 keV (gate(b)) so their time structure, when subtracted from the 1227 keV gate will strongly affect the time curve of the 1227 keV line. On the other hand, the 1173 keV line (gata(a)) is much more intense than the 1227 keV and the error introduced by using background (d) can now be neglected.

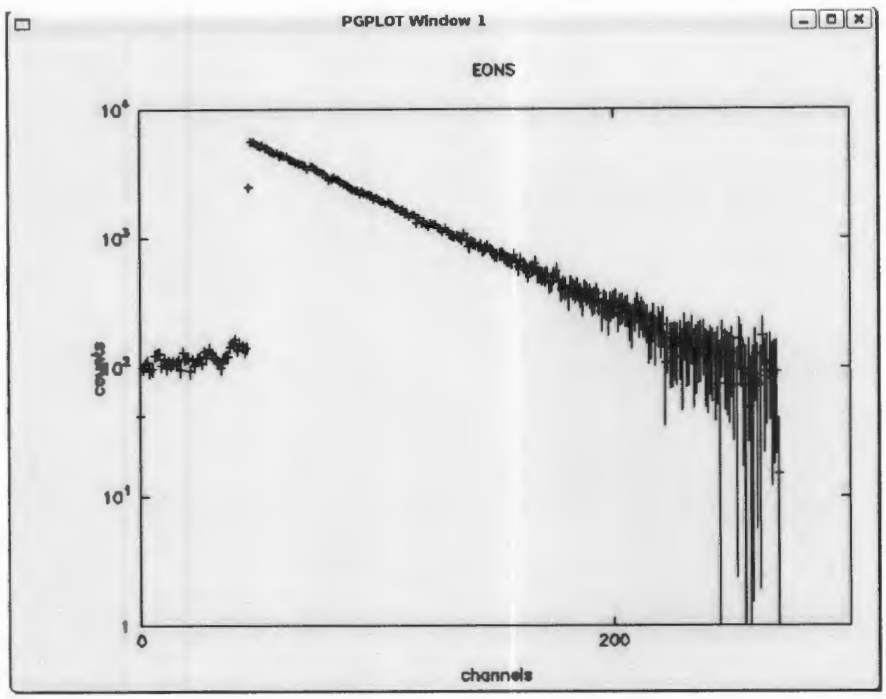

Figure 4.13: The spectrum of 243 keV γ-ray peak fitted with the program EONS.

Figure 4.15 shows the time projection of 1227 keV γ peak, the middle spectrum is the gated background from the γ-Time matrix. The spectrum at the bottom was obtained after the background subtraction has been performed. In this case the 1227 keV peak was known to be in coincidence with the 437 keV and 1525 keV γ rays and $t_1/2 = 62 \pm 1$ s was obtained using the program EONS. The Time projection spectrum in figure 4.16 is the display window obtained from the program EONS when fitting the spectrum at the bottom of figure 4.15.

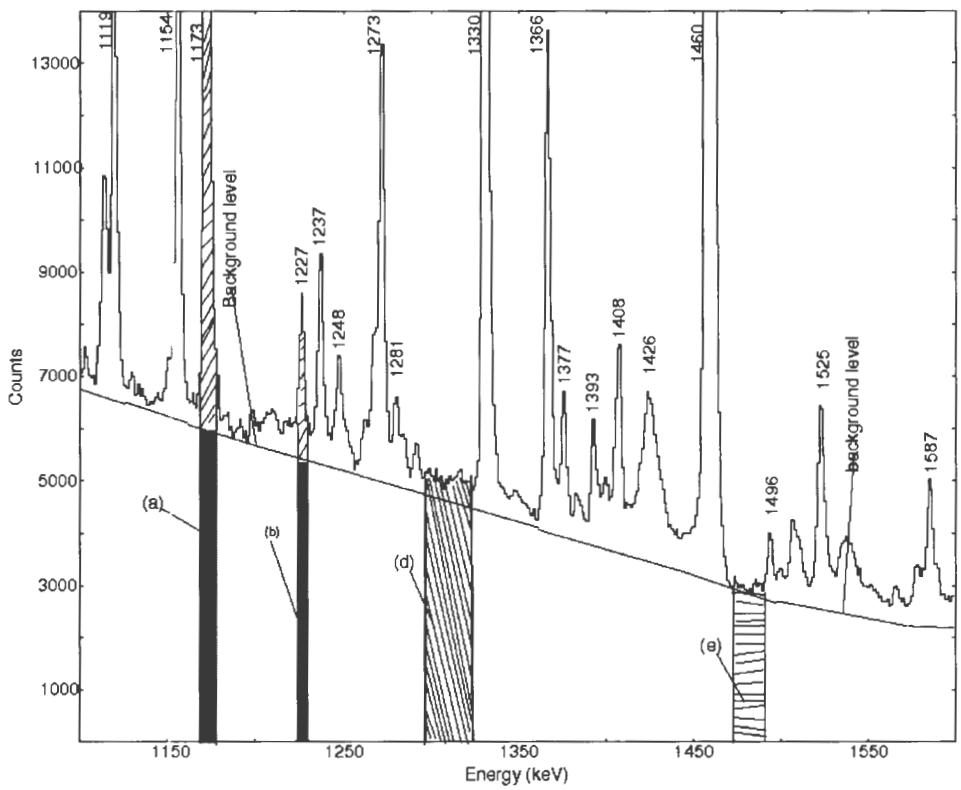

Figure 4.14: The spectrum illustrating how the gating of the area under the peak and of the background is done.

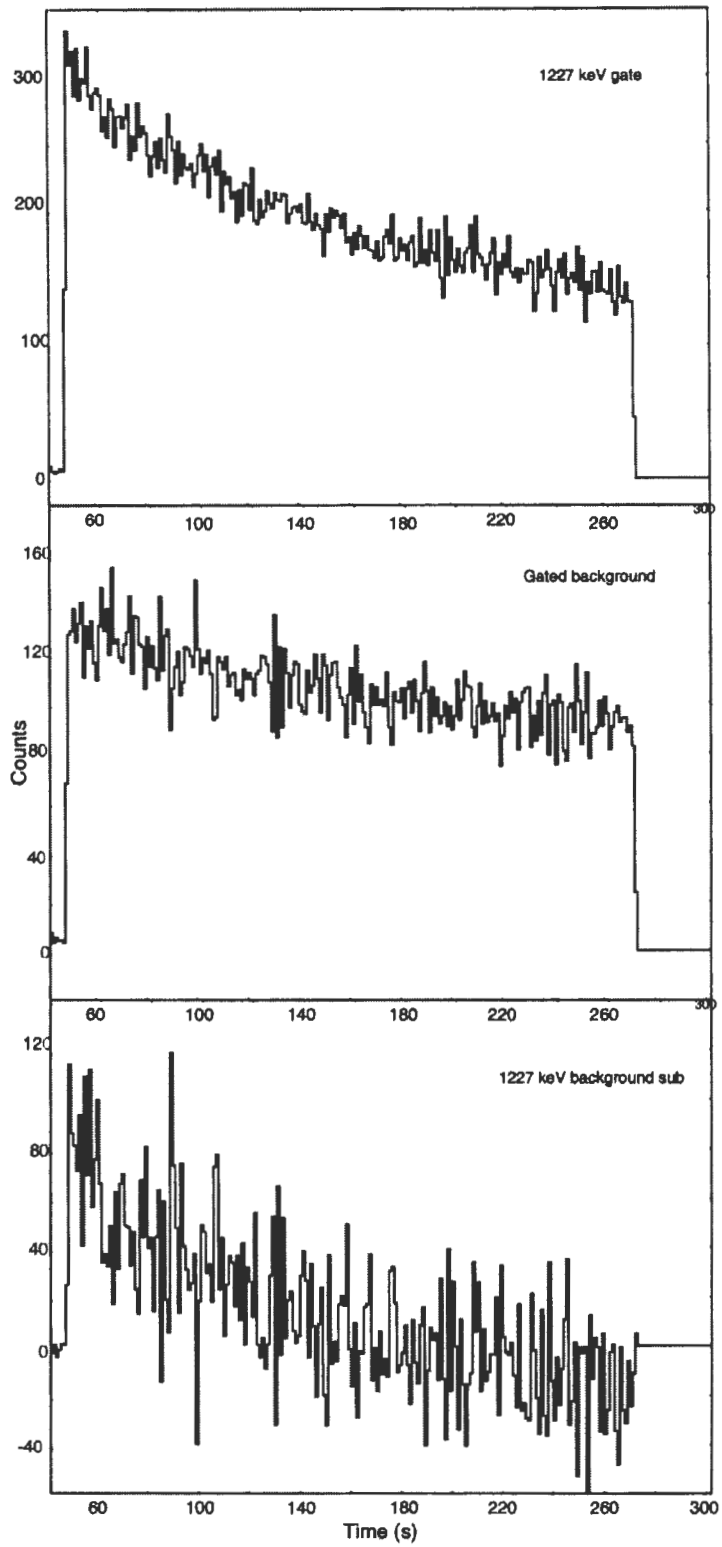

Figure 4.15: The gated peak and background spectra of the 1227 keV γ ray sliced from γ-Time matrix using program GF3. The bottom spectrum is the background subtracted spectrum.

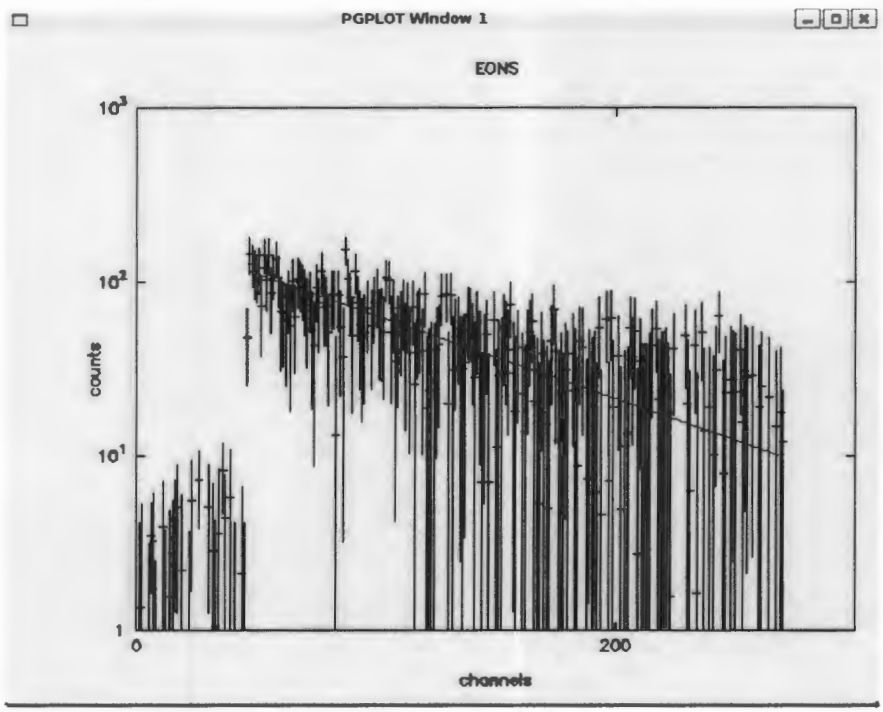

Figure 4.16: The spectrum of 1227 keV γ-ray peak fitted using the program EONS.

Chapter 5

Results of data analysis

5.1 Half-life measurement results

A summary of the half-lives measurents for each of the γ rays observed in the early-late spectrum is given in table 5.1, and are compared with the half-life measurements from previous β-decay studies. For this work the intensity I of the γ-ray has been calculated by taking the area A of the peak and dividing by the relative efficiency ε of the detector.

$$I = A/\varepsilon. \tag{5.1}$$

The uncertainty in the intensity measurements was calculated using the following equation:

$$\Delta I = I * \sqrt{\left(\frac{\Delta A}{A}\right)^2 + \left(\frac{\Delta \varepsilon}{\varepsilon}\right)^2}. \tag{5.2}$$

The area and uncertainty in the area of the peak was obtained by fitting each peak in the γ-Time projection spectrum using the Radware program GF3. The relative efficiency of the detector for each γ ray was measured from the spectrum 4.1 using the programs EFFIT and GF3. An uncertainty of 5% was used for $\frac{\Delta \varepsilon}{\varepsilon}$. The intensity and the uncertainty of all the γ rays were normalised using the intensity of the strong peak, 243 keV. The lifetimes of the new transitions in the β-decay measurements 292, 435, 1055, 1512, and 1582 keV γ ray could not be measured because the intensities of these peaks were weak in the γ-Time projection spectrum. The spin and parities of these γ rays have not been determined. In some cases there are serious differences in the intensities measured in this work compared to those of Auer *et al.* [Aue84]. Taking the average of the half-lives of transitions that are

within a factor of 2 of Auer *et al.* [Aue84], and taking an average of the others gives 35.9 s and 38.7 s respectively. This implies that the two groups have been populated mainly by one or the other of the two β-decaying states of ^{160}Lu. It is possible that these two states were populated differently in this experiment, due to the use of a much thick target (3.4 mg/cm^2 vs 1 mg/cm^2 for Auer *et al.* [Aue84]).

When the half-life is greater than 45 s the activity is identified to come from another nucleus which might be the daughters ^{160}Yb or a contaminant. The nucleus ^{160}Yb has a half-life of 288 s and it decays to its daughter ^{160}Tm which has a half-life of 74.5 s. The 132 keV γ-ray half-life was measured to be 568(4) s and is believed to come from the decay of ^{160}Yb to ^{160}Tm. The half-life of this γ ray is not the same or even close to the half-life of the parent because the measuring time (out of beam) of 225 s was short as compared to the half-life of the nucleus. The long half-lives require the use of long out OFF beam times in order to obtain accurate half-lives. In the early-late spectrum the following peaks 1632, 2113, 2203 and 2614 keV appear and the half-life was measured to be 110(8) s, 103(9) s, 1567(16) s, and 3373(19) s, respectively. This is because the half-life is too large to deduce that it belongs to ^{160}Yb, daughter or contaminant nuclei. Most of the observed γ rays identified to come from the decay of ^{160}Lu for this recent experiment were already reported in a previous study of radioactive decay of ^{160}Lu [Aue84]. The half-life measured for those γ rays was found to agree within the uncertainty.

5.2 Level scheme of ^{160}Yb

The deduced partial level scheme of ^{160}Yb, shown in figure 5.1, was constructed from the analysis of γ-γ coincidences and singles γ ray. Using the γ-γ matrix, a gate was set on 243 keV peak shown in figure 4.3. The 1512 keV peak appears as a peak that is in coincidence with it. Figure 4.4 is the spectrum gated on the 1512 keV γ-ray peak. From both spectra we see that the 1512 keV γ-ray has the same decay path as 243 keV. This confirms that the 1512 keV peak is a new transition placed in the level scheme. Using the same technique of gating into 243 keV peak, we also found the second new transition which share the same decay path with 243 keV γ ray. The 1825 keV level decays to the 243 keV level ($I = 2^+$) of the ground state band through 1582 keV γ ray.

A level has been placed at 1359 keV by Auer *et al.* [Aue84], Garret *et al.* [Gar82]. They report that it decays by three transition of 1359, 1115, and 720 keV to the $0^+, 2^+, 4^+$ levels to the ground state band, respectively. We confirm the latter two transitions in this work.

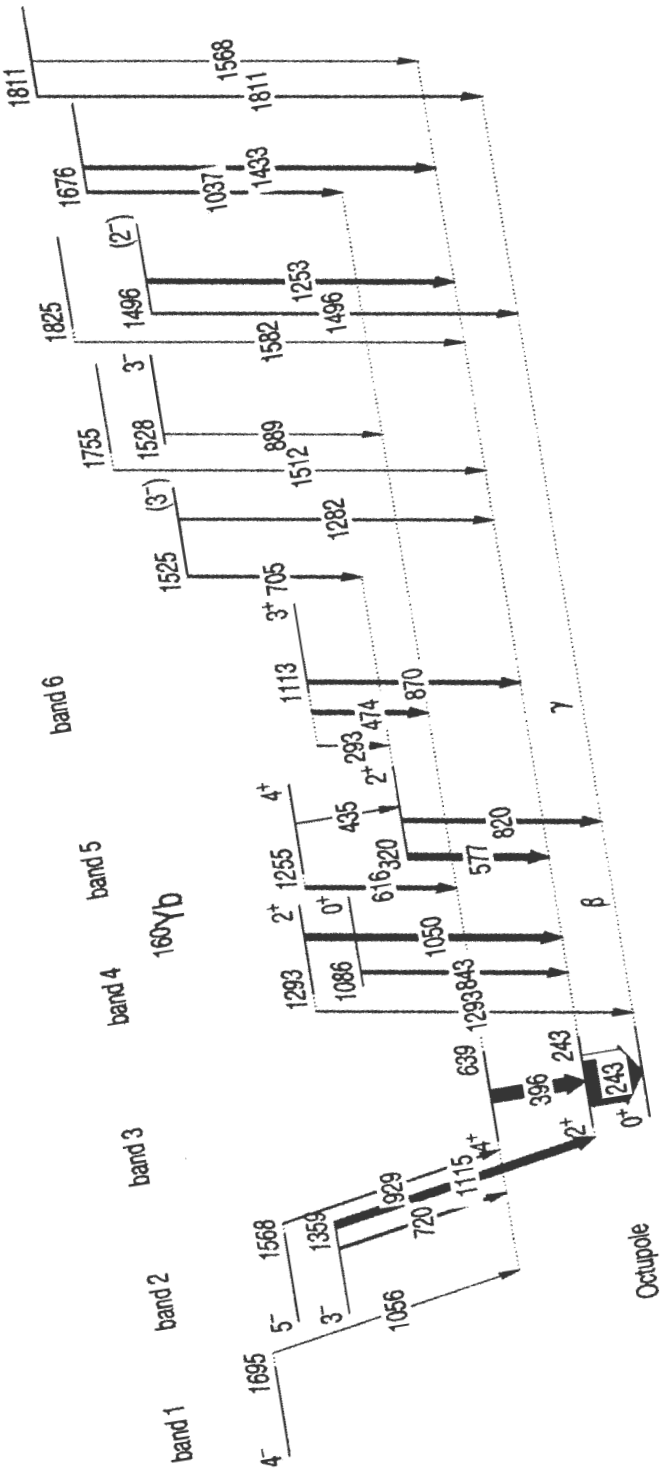

Figure 5.1: The partial level scheme of ^{160}Yb from γ-γ coincidences and γ-Time spectra. The intensities of the γ-ray transition where calculated using the equation 5.1 and their uncertainties with equation 5.2.

They assign spin and parity 2^+ to the level 1359 keV, based in part of the conversion electron measurements for the 720 keV line. However, the in-beam γ spectroscopy work places the 1359 keV level within a negative parity band (Band 5), supported by a DCO Ratio of 0.5(1) for the 1115 keV transition. Unfortunately the statistics of the in-beam γ spectroscopy experiment were insufficient to observe either the 720 or 1359 keV transitions.

The observation of the 1055 kev line places a level 1694 keV. This also coincides with the 4^- level of band 1 as seen in figure 2.5. The question arises as to whether this in fact a 4^+ level degenerate with 4^- level of band 1, in the same way that there may be degenerate 2^+ and 2^- levels. Unfortunately, the 1694 keV level is populated too weakly to see the analogs of the 720 and 1359 keV transitions, assuming similar branching ratios. The 1694 keV levels was not observed in Auer *et al.* [Aue84] or Garret *et al.* [Gar82] work.

The 1811 keV level is the other level observed in the β-decay measurements [Aue84] and not in the in-beam γ spectroscopy. This level decays with 1811 keV γ ray to the ground state ($I^\pi = 0^+$) and a 1568 keV γ ray to the first excited 2^+ state of the ground band. Band 9 from in-beam γ spectroscopy measurements (see figure 2.5) has 1294 keV level which decays to the 0^+ level of the ground state band and it was identified to be the $K = 0$ β vibrational band [Mal06]. In the same band the 1086 keV level was not confirmed because of the intensity of the γ was weak. We confirm and improve the latter two levels in this work because we have observed the decay transition from 1086 keV level to 243 keV level of the ground state band through 843 keV γ ray.

The 1113 keV level de-excites through the 293 keV γ ray to the $I^\pi = 2^+$ state of the γ-vibrational band, through the 474 keV γ ray to the $I^\pi = 4^+$ state of the ground state band, and through the 870 keV γ ray to the $I^\pi = 2^+$ state of the ground state band. The level at 820 keV decays with two transitions, 820 keV γ ray decays to the $I^\pi = 0^+$ state and the 577 keV γ ray decays to the first excited $I^\pi = 2^+$ state. The 435 keV and 616 keV transitions deexcite the 1255 keV level into the 639 keV level ($I^\pi = 4^+$) of the ground state band and the 820 keV ($I^\pi = 2^+$) level respectively. The level at 820 keV is strongly populated from the decay of ^{160}Lu and it is the lowest observed state that does not belong to the ground state band.

In the γ-γ matrix it was found that the 437, 1227 and 1525 keV γ rays are in coincidence with each other, and they also appeared in the early-late spectrum. From this we expect these γ rays to have the same lifetime. The 437 keV γ-ray peak has more statics compared to the 1227 and 1525 keV peaks. We have measured the half-lives of 437, 1227, and 1225 keV peak to be 58.18 ± 1.09 s, 62 ± 1 s and 60 ± 1 s respectively. This confirmed our expectation

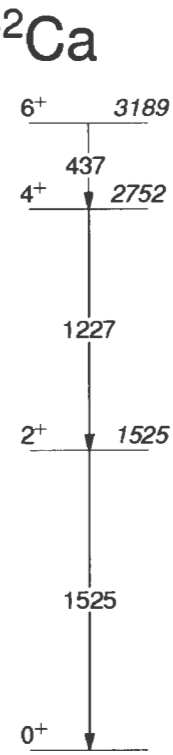

Figure 5.2: Level scheme of ^{42}Ca deduced in the present work.

of getting the same half-life for all the peaks that are in coincidence. These γ rays were emitted from the β^+-decay of the nucleus ^{42}Sc to ^{42}Ca. The nucleus ^{42}Sc, with a half-life of 61 s, was created in the ^{27}Al(^{19}F,p3n)^{42}Sc reaction, which means that during the experiment the ^{19}F beam hit the Aluminium target frame. The level scheme of ^{42}Sc shown in figure 5.2.

5.3 Discussion

Two beta-decaying states of ^{160}Lu with half-lives of 36.2(3) and 40(1) s were reported by Auer *et al.* [Aue84]. The present measurements also give half-lives typically between 36 s and 40 s as seen in table 5.1, but differ in the details of which states belong to the 36 s half-life and which to the 40 s. For example, the 396 keV transition is measured here to have a half life of 36.5(6) s, compared with that measured by Auer *et al.* [Aue84] of 40(1) s.

The spin and parities of the β-decaying states in ^{160}Lu were assigned to be $I^\pi = 1^-$ and $I^\pi =$

4^-, [Aue84]. This was explained by Auer *et al.* [Aue84] using the Nilsson model for protons and neutrons. They argued that for ^{160}Lu with $Z = 71$ and $N = 89$, the lowest available proton orbitals are $\frac{1}{2}^+[411]$ and $\frac{5}{2}^-[402]$, (these two Nilsson orbitals have been claimed to be the main configuration of the parent states in ^{164}Lu and in ^{166}Lu [Hun77, Boe74]), while for the unpaired neutron possible single particle orbitals are the $\frac{1}{2}^+[660]$ and the $\frac{3}{2}^-[521]$ orbitals. Since the residual proton-neutron interaction favours a parallel coupling of the intrinsic spins of the proton and neutron, the favoured combinations of these states are expected to be $\frac{1}{2}^+[411] \otimes \frac{3}{2}^-[521]$; 1^- and $\frac{5}{2}^-[402] \otimes \frac{3}{2}^-[521]$; 4^-. Auer *et al.* [Aue84] then argued that the 4^- state populated the higher spin states (with the 40 s half-life) and the 1^- (with the half-life of 36 s) those at lower spin.

Certainly, when one uses the measured lifetimes, intensities and the tables of Gove and Martin [Gov71] to calculate the log ft values, one can see that log ft values for the this work is in the range $\sim$ 6-7 as shown in table 5.2, consistent with allowed and first-forbidden transitions.

Taking this information together with the in-beam γ spectroscopy results, the following configuration assignments are suggested:

5.3.1 Band 1 and Band 2

The negative parity side bands have been interpreted as the low-lying members of octupole vibrational bands [Mal06]. These octupole vibrational bands are constructed on the level scheme of ^{160}Yb in figure 5.1 and are observed in the in-beam γ spectroscopy measurements 2.5.

5.3.2 Band 3

Only two transitions of the ground state band were observed as shown in figure 5.1. This is consistent with the suggested [Aue84] spin and parity assignment of the β-decay states in ^{160}Lu.

5.3.3 Band 4

Band 4 is likely to be the $K = 0$ β vibrational band. The 0^+ state was not identified in the in-beam γ spectroscopy measurements due to the loss of intensity (see figure 2.5), but in

this present work we confirm the existance of the level with the observation of the 843 keV transition. The configuration assignment of this level is based on the systematics [Mal06].

5.3.4 Band 5 and Band 6

Band 5 and 6 were identified [Mal06] as the low spin member of the γ band.

In figure 5.1, the remaining levels are likely to be vibrational states, as the energies of these levels are less than 2.48 MeV (obtained from the calculations of the pairing gap parameter [Ben86] using the tables of Wapstra and Bos [Wap77]), still too low to associate them with two quasi-neutron states. None of the structures can readily be identified with a tetrahedral shape.

	Present work		Auer *et al.* [Aue84]			
E_γ (keV)	I_γ	$T_{1/2}$ (s)	I_γ	$T_{1/2}$ (s)	States:$j_i \rightarrow J_f(\hbar)$	Nucleus
140.2(1)	30.2(1.5)	88(1)			$0^+, 1^+, 2^+ \rightarrow 1^-$	^{160}Tm
173.8(1)	114.4(5.7)	507(2)			$1^+ \rightarrow 2^-$	^{160}Tm
215.8(1)	51.6(2.6)	481(3)			$1^+ \rightarrow 1^-$	^{160}Tm
243.4(1)	100(5.0)	35.5(3)	100.0	36.2(3)	$2^+ \rightarrow 0^+$	^{160}Yb
292.5(3)	0.18(0.3)		1.0(1)	36(2)	$5^+ \rightarrow 2^+$	^{160}Yb
372.7(1)	65.9(3.3)	1062(7)			$1^+ \rightarrow 1^+$	^{160}Tm
395.5(1)	28.0(1.4)	36.5(6)	21.0(9)	40(1)	$4^+ \rightarrow 2^+$	^{160}Yb
434.3(1)	0.7(0.04)		1.0(2)	31(4)	$3^- \rightarrow 2^+$	^{160}Yb
436.8(1)	0.8(0.2)	58(2)			$6^+ \rightarrow 4^+$	^{42}Ca
474.4(1)	0.74(0.4)	43(3)	1.1(1)	38(3)	$3^+ \rightarrow 4^+$	^{160}Yb
577.1(1)	13.6(0.7)	36.1(2)	10.7(8)	36(1)	$2^+ \rightarrow 2^+$	^{160}Yb
616.2(1)	7.2(0.4)	43(3)	1.7(3)	43(4)	$3^- \rightarrow 4^+$	^{160}Yb
704.6(1)	4.2(0.3)	39(2)	2.7(2)	41(2)	$1^-, 2^-3^- \rightarrow 2^+$	^{160}Yb
719.8(1)	4.4(0.4)	38(2)	0.8(1)	30(4)	$2^+ \rightarrow 4^+$	^{160}Yb
820.1(1)	7.7(0.4)	40(1)	6.1(5)	35(1)	$2^+ \rightarrow 2^+$	^{160}Yb
843.3(1)	6.5(0.4)	36(4)	2.1(4)	48(8)	$(0)^+ \rightarrow 2^+$	^{160}Yb
869.9(1)	7.4(0.5)	29(6)	6.2(5)	35(1)	$3^+ \rightarrow 2^+$	^{160}Yb
929.1(1)	2.3(0.2)	30(8)	0.7(2)	40(8)	$(3^- \rightarrow 4^+$	^{160}Yb
1008.4(1)	12.4(1.0)	213(12)			$2^+ \rightarrow 0^+$	^{160}Er
1037.5(1)	4.6(0.2)		0.8(2)		$(2^+, 3, 4^+) \rightarrow 4^+$	^{160}Yb
1050.3(1)	13.3(0.7)	36(2)	1.8(3)	43(4)	$2^+ \rightarrow 2^+$	^{160}Yb
1055.2(1)	1.79(0.3)			$4^- \rightarrow 4^+$	^{160}Yb	
1114.9(1)	16.5(0.9)	30.9(9)	6.8(5)	39(1)	$2^+ \rightarrow 2^+$	^{160}Yb
1172.9(1)	105.0(5.3)	1477(10)			$4^+ \rightarrow 2^+$	^{60}Ni
1227.0(1)	9.4(0.5)	62(1)			$4^+ \rightarrow 2^+$	^{42}Ca
1253.4(2)	5.42(0.4)	36(2)	1.0(3)	25(5)	$(1, 2^+) \rightarrow 2^+$	^{160}Yb
1272.6(1)	33.5(1.7)	499(5)			$2^- \rightarrow 2^+$	^{160}Dy
1282.0(1)	3.0(0.2)	41(4)	0.5(2)	41(5)	$(2)^- \rightarrow 2^+$	^{160}Yb
1286.4(2)			0.4(1)	65(13)	$(3)^- \rightarrow 2^+$	^{160}Yb
1292.6(1)	1.8(0.2)	38(3)	1.1(2)	39(4)	$2^+ \rightarrow 0^+$	^{160}Yb
1332.8(1)	3.9(0.4)	135(6)			$2^+ \rightarrow 0^+$	^{60}Ni
1432.9(1)	5.4(0.4)	38(8)	0.5(3)	53(21)	$(2^+, 3, 4^+) \rightarrow 2^+$	^{160}Yb
1460.3(1)	432.2(21.6)	2222(11)			$\rightarrow 0^+$	^{160}Er,^{40}K
1496.3(2)	3.5(0.2)	35(3)	1.5(2)	31(3)	$(1, 2^+) \rightarrow 0^+$	^{160}Yb
1512.4(1)	0.57(0.06)					^{160}Yb
1524.7(1)	18.2(0.9)	60(1)			$2^+ \rightarrow 0^+$	^{42}Ca
1568.2(3)	1.4(0.2)	30(3)	1.3(4)	28(4)	$(1, 2)^+ \rightarrow 0^+$	^{160}Yb
1582.2()	2.25(0.4)					^{160}Yb
1778.0(1)	243.7(12.2)	147.0(9)			$(1, 2, 3)^- \rightarrow 2^+$	^{40}Ar
1810.8(1)	2.6(0.3)	42(3)	0.5(2)	26(6)	$(1, 2^+) \rightarrow 0^+$	^{160}Yb

Table 5.1: Spectroscopic data of γ transitions in ^{160}Yb. The relative intensities normalised to 100 for the 243 keV γ ray. The empty spaces is due to unobserved γ rays by Auer *et al.* [Mal06] experiment or in this experiment. The error limits include uncertainties in the peak areas and in the detector efficiency calibration.

E_γ (keV)	I_γ	logft	$T_{1/2}$ (s)
243.4(1)	100.0	7.23	35.5(3)
395.5(1)	28.0(1.4)	6.80	36.5(6)
474.4(1)	0.74(0.4)	6.76	43(3)
577.1(1)	13.6(0.7)	7.49	36.1(2)
616.2(3)	7.2(0.4)	6.76	43(3)
704.6(1)	4.2(0.3)	6.65	39(2)
719.8(1)	4.4(0.4)	6.71	38(2)
820.1(1)	7.7(0.4)	6.858	40(1)
843.3(1)	6.5(0.4)	6.95	36(4)
869.9(1)	7.4(0.5)	6.85	29(6)
929.1(2)	2.3(0.2)	6.73	30(8)
1050.3(1)	13.3(0.7)	6.89	36(2)
1114.9(1)	16.5(0.9)	6.85	30.9(9)
1253.4(2)	5.42(0.4)	6.82	36(2)
1282.0(1)	3.0(0.2)	6.67	41(4)
1292.6(1)	1.8(0.2)	6.71	38(3)
1432.9(1)	5.4(0.4)	6.58	38(8)
1496.3(2)	3.5(0.2)	6.59	45(2)
1568.2(3)	1.4(0.2)	6.68	30(3)
1810.8(1)	2.6(0.3)	6.62	42(3)

Table 5.2: Energies, intensities, log ft values and the half-life for states in ^{160}Yb populated by 160Lu.

Chapter 6

Conclusions

In this work, the search for non-yrast states of ^{160}Yb has been conducted by observing the β-decay of ^{160}Lu. The computer program EONS, used to measure the half-lives of the γ rays, was successful in determining the correct half-lives for γ rays originating from the short-lived ^{160}Lu and long-lived ^{42}Sc states. The results obtained does not preciously distinguish the two isomers of ^{160}Lu differently as reported by Auer *et al.* [Aue84]. The half-life of ^{42}Sc was found to be around 61 s and it agrees with the measurements performed previously in the beta-decay of ^{42}Sc to ^{42}Ca [Del78]. It can be seen from the table 5.1 that we have done well in identifying almost all of the strong peaks populated in this experiment. Actually, we wanted to improve the previous β^+-decay measurements and the in-beam γ spectroscopy data, since we have the AFRODITE array with high relative efficiency of measuring high energy γ rays. Indeed, we managed to observe two new levels; the 1755 keV level decays through 1512 keV and the 1825 kev level decays through 1582 keV γ ray to the 243 keV 2^+ state of the ground state band. The decay of 1086 keV level through 843 keV γ ray to 243 keV level of the ground state band has been confirmed and we observed the transition 1055 keV from 1694 keV level which was previously found in the in-beam γ spectroscopy measurements and not in the β-decay studies. It is planned to propose another measurement to increase statistics sufficiently to see any possibly transitions to the 6^+ and 2^+ levels from the levels at 1694 keV. Finally, we can say the low spin states of ^{160}Yb have been successfully populated through the EC or β^+-decay of ^{160}Lu.

Appendix A

Appendix

A.1 Convolution Program

Date: 8 October 2007
Author: T. D. Singo
This program simulates the β^+-decay chain of the nucleus with mass number $A = 160$. The plots in figure 3.6, 3.7 and 3.8 are plotted using this program. It is written in matlab language.

```
L=[0.693/38, 0.693/(4.8*60), 0.693/(9.4*60),0.693/(28.58*60*60),0.693/(5.02*60)];

t=1:200000;
a=45;
U=ones(size(t));
U(1:a)=0;
total= zeros(4,length(t))
n=zeros(4,length(t));   %allocate the storage for 4 graphs,with different time
C=ones(4,4);            %storing the constant Cmax of i=4 so Cmax=5
for i=1:4
pL=prod(L(1:i-1))   %calculating the products for L
for k=1:i
for j=1:i
```

```
if j~=k
C(k,i)=C(k,i)/(L(j)-L(k));    % calculating constant Cki product
end
end
n(i,:)=n(i,:)+pL*C(k,i)/L(k)*(1-exp(-L(k)*t) - U.*(1 - exp(-L(k)*(t-a))));
end
end

for p=0:7000
for tt=(p*270+1):200000
total(:,tt)=total(:,tt)+n(:,tt-p*270);
end
end
figure;hold on;
for i=1:4
plot(t,total(i,:))
end

figure;hold on;
for i=1:4
plot(t,n(i,:))
end
```

Bibliography

[Aue84] Auer, H. *et al.*, *Zeitschrift für Physik A*, **318**, 323 (1984).

[Bar05] Bark, R. *et al.*, *Journal of Physics G: Nuclear and Particle Physics*, **31**, s1747-s1752 (2005).

[Ben86] Bengtsson, S. and Frauendorf., *Atomic Data and Nuclear Data tables*, Volume **35**, no 1, 176 (1986).

[Berl80] Berlovich, E. Ye. *et al.*, *Acta Physics Polonica B* Volume **11**, 455 (1980)

[Bla52] Blatt, M. J., and Weisskopf, V. F., *Theoretical Nuclear Physics*, John Wiley & sons, United States of America (1952).

[Blin91] Blin-stoyle, R. J., *Nuclear and Particle Physics*, Chapman & Hall (1991).

[But00] Butler, P. A., *Physica scripta*, **T88**, 7-9, (2000).

[BruRoo] Brun. R. and Rademakers F., *An ObjectOriented Data Analysis Framework* http://root.cern.ch/root/Version514.html

[Byr87] Byrski, T. *et al.*, *Nuclear Physics A*, *474*, 193-218 (1987).

[Cam04] Campbell, D. B., *PhD thesis*, Florida State University College of Arts and Sciences, Tallahassee, Florıda (2004).

[Boe74] De Boer, F. W. N. *et al.*, *Nuclear Physics*, **A225**, 317-351(1974).

[Del78] Delvecchio, R. M., and Daehnick, W. W., *Physical Review C*, **17** 1809-1814 (1978).

[Duc99] Duchene, G. *et al.*, *Nuclear Instruments and Methods A*, **432** 90 (1999).

[Dud02] Dudek, J. *et al.*, *Physical Review Letters*, **88**, 252505 (2002).

[Dud03] Dudek, J. *et al.*, *arXiv:nucl-th/0303001*, Volume 1, (2003).

[Dud06] Dudek, J. *et al.*, *Physical Review Letters*, **97**, 072501 (2006).

[Dud07] Dudek, J. *et al.*, *Acta Physica Polonica B* Volume **38**, no 4, 1389 (2007)

[Eis87] Eisenberg, J. M. and Greiner, W., *Nuclear Theory vol 1: Nuclear Models*, 3rd edition, North-Holland (1987).

[Fir96] Firestone, R. B. and Shirley, V. S., *Table of Isotopes*, Volumes I and II, 8th edition, John Wiley & sons, New York (1996).

[Gar82] Garrett, C. *et al.*, *Physical Review Letters B*, **118**, 292 (1982).

[Gov71] Gove, N. B. and Martin, M. J., *Nuclear Data tables*, Volume **10**, no 3, 260(1971).

[Gre98] Greenlees, P. T., *Journal of Physics G: Nuclear and Particle Phyiscs*, **24**, L64 (1998).

[Hil80] Hillman, M. and Eyal, Y., http://dnr080.jinr.ru/lise/5_13/lise_ 5_13.html (1980)

[Hun77] Hunter, R. C *et al.*, *Physical Review C*, volume **16**, no 1, 384(1977).

[Jon95] Jones, P. M. *et al.*, *Nuclear Instruments and Methods A*, **362**, 556-560 (1995).

[Kno00] Knoll, G. F., *Radiation Detection and Measurement*, 3rd edition, John Wiley & Sons, New York (2000).

[Kra88] Krane, K. S., *Introductory Nuclear Physics*, John Wiley & Sons, 2nd edition, Canada (1988).

[Led67] Lederer, C. *et al.*, *Table of Isotopes*, 6th Edition, John Wiley & sons (1967).

[Leo87] Leo, W. R., *Techniques for Nuclear and Particle Physics Experiments*, 2nd edition, Springer-Verlag, New York and Berlin (1987).

[Lil01] Lilley, J. S., *Nuclear Physics*, John Willey & Sons, England (2001).

[Mab03] Mabala, G. K., *PhD thesis*, University of Cape Town, Cape Town, South Africa (unpublished) (2003).

[Mal06] Maliage, S. M., *MSc thesis*, University of Western Cape, Bellville, South Africa (unpublished) (2006).

[Nil95] Nilsson, S. G. and Ragnarsson, I., *Shapes and Shells in Nuclear Structure*, Cambridge (1995).

[Nts05] Ntshangase, S. S., *MSc Thesis*, University of Zululand, Kwazulu Natal, South Africa (unpublished)(2005)

[Pov02] Povh, B, *et al.*, *Particles and Nuclei, An Introduction Physical Concepts*, 3rd edition, Springer-Verlag Berlin Heidelberg, Germany (2002).

[Rad95] Radford, D. C., ESCL8R and LEVIT8R: Software for Interactive Graphical Analysis of HpGe Coincidence Data Sets. *Nuclear Instruments Methods in Physiscs A* **361**, 297 (1995).

[Rie80] Riedinger, L. L. *et al.*, *Physical Review Letters*, **44**, no 9, 569 (1980).

[Sat80] Satchler, G. R , *Introduction to Nuclear Reactions*, Macmillan Press ltd, London and Basingstoke (1980).

[Sch04] Schunck, N. *et al.*, *Physical Review C* **69**, 061305 (2004).

[Sha88] Sharpey-Schafer, J. F. and Simpson, J., *Progress Particle Nuclear Physics*, **21** 293-400(1988).

[SamMTsort] Sampson, J. and Cresswell, J., *Nuclear Physics Research Group Software-MTsort Sorting Program*, http://ns.ph.liv.ac.uk/MTsort-manual/MTsort.html.

[Wap77] Wapstra, A. H. and Bos, K., *Atomic Data and Nuclear Data tables*, Volume **19**, no 3, 175(1977).